eprints@whiterose.ac.uk
https://eprints.whiterose.ac.uk/

HST and UKIRT imaging observations of $z \sim 1$ 6C radio galaxies – II. Galaxy morphologies and the alignment effect

K. J. Inskip,[1,2][*] P. N. Best,[3] M. S. Longair[2] and H. J. A. Röttgering[4]

[1]*Department of Physics & Astronomy, University of Sheffield, Sheffield S3 7RH*
[2]*Cavendish Laboratory, Madingley Road, Cambridge CB3 0HE*
[3]*Institute for Astronomy, Royal Observatory Edinburgh, Blackford Hill, Edinburgh EH9 3HJ*
[4]*Sterrewacht Leiden, Postbus 9513, 2300 RA Leiden, the Netherlands*

ABSTRACT

Powerful radio galaxies often display enhanced optical/ultraviolet emission regions, elongated and aligned with the radio jet axis. The aim of this series of papers is to investigate separately the effects of radio power and redshift on the alignment effect, together with other radio galaxy properties. In this second paper, we present a deeper analysis of the morphological properties of these systems, including both the host galaxies and their surrounding aligned emission.

The host galaxies of our 6C subsample are well described as de Vaucouleurs ellipticals, with typical scale sizes of $\sim$10 kpc. This is comparable to the host galaxies of low-z radio sources of similar powers, and also the more powerful 3CR sources at the same redshift. The contribution of nuclear point source emission is also comparable, regardless of radio power.

The 6C alignment effect is remarkably similar to that seen around more powerful 3CR sources at the same redshift in terms of extent and degree of alignment with the radio source axis, although it is generally less luminous. The bright, knotty features observed in the case of the $z \sim 1$ 3CR sources are far less frequent in our 6C subsample; neither do we observe such strong evidence for evolution in the strength of the alignment effect with radio source size/age. However, we do find a very strong link between the most extreme alignment effects and emission-line region properties indicative of shocks, regardless of source size/age or power. In general, the 6C alignment effect is still considerably stronger than that seen around lower redshift galaxies of similar radio powers. Cosmic epoch is clearly just as important a factor as radio power: although aligned emission is observed on smaller scales at lower redshifts, the processes which produce the most extreme features simply no longer occur, suggesting considerable evolution in the properties of the extended haloes surrounding the radio source.

Key words: galaxies: active – galaxies: evolution – galaxies: ISM – radio continuum: galaxies.

1 INTRODUCTION

Powerful radio galaxies at $z > 0.3$ are often observed to be surrounded by extensive regions of ultraviolet (UV)/optical continuum and line emission. The excess continuum emission is generally well aligned with the radio source axis at higher redshifts ($z \gtrsim 0.6$), and is known as the *alignment effect* (e.g. Chambers, Miley & van 1987; McCarthy et al. 1987).

The extended emission regions responsible for the alignment effect have been well studied in the case of powerful radio galaxies selected from the 3CR sample (e.g. McCarthy, Spinrad & van Breugel 1995; Best, Longair & Röttgering 1997). Whilst a wide range of different features are observed for the extended emission surrounding this sample of radio galaxies, several clear trends are generally observed. At higher redshifts ($z \sim 1$), the optical/UV emission is typically brighter than at lower redshifts, and can be more luminous than the host galaxy in some cases. This emission is also typically more extensive, with projected linear sizes of up to a few hundred kpc, and is far more closely aligned with the radio source axis than is the case for lower redshift systems. The emission surrounding the less powerful 3CR radio sources at lower redshifts is rarely as extensive, and with the exception of ionization cones produced by the powerful obscured active galactic nucleus (AGN), does not usually display any tendency for alignment with the radio axis (Allen et al. 2002). For the high-redshift 3CR sources, the alignment effect also displays a strong trend with radio source size; smaller sources typically display the most extensive, luminous aligned emission regions (Best, Longair & Röttgering 1996).

[*]E-mail: k.inskip@shef.ac.uk

© 2005 RAS

Multiwavelength observations have shown that a number of different emission mechanisms are responsible for this extended excess UV/optical emission. These include extended line emission and nebular continuum radiation (Dickson et al. 1995), scattering of the UV continuum from the AGN (e.g. Tadhunter et al. 1992; Cimatti et al. 1993) and young stars produced in a radio jet induced starburst (McCarthy et al. 1987). The relative contributions of each of these processes vary from source to source, and generally the excess emission cannot be accounted for by any single mechanism. It is clear from the observed trends that not only do different processes vary in importance at different stages of the life of a given radio source, but that the mechanisms which produce the excess emission also vary with redshift. However, it is not obvious whether this evolution in the properties of the emission regions surrounding the 3CR sources reflects a genuine evolutionary trend with redshift, or if it is instead owing to the decreasing radio power of the lower redshift systems. With such strong apparent links between the radio source and the aligned/excess emission, both in terms of the morphology and emission properties of the alignment effect, the necessity for breaking this degeneracy is clear.

The 6C sample provides an ideal population of radio galaxies which, in conjunction with the well-studied 3CR sample, can be used to break the degeneracy between redshift and radio source power present in studies of a single flux limited radio galaxy sample. At $z \sim 1$ the 6C radio sources are typically ~ 6 times less powerful than the 3CR sources at the same redshift, and matched in radio power to 3CR sources at lower redshifts of $z \sim 0.2$–0.5. Deep spectroscopic observations of $z \sim 1$ 6C sources have enabled the importance of cosmic epoch and the radio source parameters on the properties of the extended emission-line structures to be determined independently (Inskip et al. 2002b,c). These studies were able to demonstrate that both radio power and redshift were independently important for the kinematic properties of the gas, but that ionization state only depended on the radio source parameters and not on redshift. We now intend to use the same samples to address the question of the evolution of the morphological properties of these systems, as many of the mechanisms by which aligned continuum emission can be produced are also highly dependent on the properties of the radio source and AGN.

In order to correctly interpret the properties of the aligned emission regions, it is also necessary to have a thorough understanding of the host galaxy morphologies. It is therefore important to determine the structural parameters of the host galaxies precisely, particularly with regard to the presence of an unresolved point source contribution from an incompletely obscured AGN. For the later consideration of galaxy colours, this AGN contribution must be included in the excess UV emission, which does not necessarily originate wholly from any external alignment effect.

At redshifts of up to at least $z \sim 1$, the host galaxies of the powerful 3CR radio sources are usually found to be giant ellipticals with characteristic sizes of ~ 10–12 kpc (Best, Longair & Rottgering 1998; McLure & Dunlop 2000), and are amongst the most massive galaxies known at high redshifts. The stellar populations of these galaxies are also amongst the oldest found; the K-band magnitude–redshift relation for the most powerful 3CR radio sources is consistent with passively evolving galaxies with old stellar populations formed at $z \sim 5$ or earlier. More varied morphologies are observed at higher redshifts where the host galaxies may still be in the process of formation (e.g. Pentericci et al. 1999). The 6C radio galaxy sample, selected at a lower limiting radio flux density than the 3CR sample, displays a similar K–z relation at low z. However, beyond $z \sim 0.8$, the K magnitudes of these sources are typically ~ 0.6 magnitudes fainter (Eales

& Rawlings 1996), a variation between the samples which can be interpreted in several ways (Inskip et al. 2002a). The more luminous galaxies could have a greater AGN contamination in their K-band magnitudes from direct nuclear light, emission lines or other AGN-induced emission; the stellar populations of the different samples could differ in age or metallicity; or more simply, the less powerful high-z radio sources could be hosted by less massive galaxies. A mass difference can be easily understood: if the radio sources are being fuelled at the Eddington limit then the radio power depends upon black hole mass, and it is now well established that black hole mass and galaxy mass are correlated (Kormendy & Richstone 1995). An early study of the host galaxies of $z \sim 1$ 6C sources (Roche, Eales & Rawlings 1998, hereafter RER98) suggested that they are typically hosted by elliptical galaxies with a far smaller average physical size than 3CR sources at the same redshift. However, as this result was based upon measurements of galaxy sizes <1 arcsec with 0.5 arcsec pixels in 1.5-arcsec seeing conditions, confirmation of this result using improved instrumentation was certainly desirable.

In the first paper in this series (Inskip et al. 2003, hereafter Paper I), we presented the results of *HST* and UKIRT imaging observations of a complete sample of $z \sim 1$ 6C radio galaxies. Full details of the sample selection and observations are provided within that paper. In this paper, we study the morphologies of the host galaxies and the aligned emission regions in greater depth. The results of two-dimensional (2D) modelling of the K-band morphologies of the host galaxies are presented in Section 2, through which we have deduced the structural parameters for the host galaxies, including any contribution from an incompletely obscured nuclear point source component. The resulting radial profiles, characteristic radii, ellipticity and percentage contribution of unresolved nuclear emission are contrasted with the results of other radio galaxy samples. In Section 3, we quantify various properties of the aligned emission on the basis of the elongation and orientation of the rest-frame UV aligned structures visible in our *HST* observations. The properties of the 6C subsample are compared with the data for the matched 3CR sample at the same redshift. The behaviour of the aligned emission is studied as a function of both radio source size and redshift, as well as over the factor of ~ 6 difference in radio power between the two samples. In Section 4, we discuss the range of different morphologies observed in the two samples, and the implications of these combined results. In the third paper in this series, we will present a detailed study of the galaxy colours for both $z \sim 1$ subsamples. Cosmological parameters of $\Omega_0 = 0.3$, $\Omega_\Lambda = 0.7$ and $H_0 = 65$ km s^{-1} Mpc^{-1} are assumed throughout this paper.

2 GALAXY MORPHOLOGIES

2.1 Properties of the host galaxies

Our deep K-band observations of the 6C sources (with a limiting 1σ magnitude of $K \sim 23.4$ arcsec^{-2}) are particularly well suited to the study of the host galaxy morphologies, through the fitting of their radial/surface profiles. In order to carry out this fitting, it was first necessary to obtain accurate point source profiles for each of the fields. The observations for each individual source were carried out over several nights under quite variable seeing conditions (ranging from 0.4 to 1.2 arcsec; see Paper I for full details). The point spread functions (PSFs) for each source are therefore quite complex, and are best reproduced by extracting 2D profiles for all stars in the field of each source, normalizing to unit flux and taking the average profile. As a guideline, the average seeing for each source ranges from 0.6 to 0.9 arcsec, with a mean value for the sample as a whole

of 0.75 arcsec. In order to accurately model the galaxies, nearby objects were masked where these were well separated from the host galaxy; where this was not possible (e.g. 6C 1100+35, 1129+37 and 1256+36) a second galaxy and/or point source is included in our modelling to account for the extra flux from the secondary object. Galaxy models were then convolved with these PSFs and used to fit the surface profiles of the galaxies, using available least-squares minimization IDL routines. In particular, we have made use of the IDL (interactive data language) routine MP2DFUNFIT.PRO, part of the MPFIT IDL package.[1] The MPFIT package iteratively searches for the best-fitting model parameters via minimization of the weighted squared difference between the data and model. This least-squares minimization uses the Levenberg–Marquardt technique (More 1977), which numerically calculates the derivatives of the assumed function/model via a finite difference approximation (for further details, see More & Wright 1993 and MINPACK-1, available from netlib at http://www.netlib.org). In order to weight the data at different radii uniformly, rather than giving preference to either the higher signal-to-noise (S/N) ratio data at the centre of each galaxy or the lower S/N ratio data at larger radii for which we have more pixels, we have weighted each pixel by $1/2\pi r$, normalizing the weights to a mean value of 1.0 so as not to alter the resulting value of χ^2 produced by the code. We have determined that this weighting scheme does not introduce any strong biases into the fitting procedure. Formal 1σ uncertainties on each parameter are computed from the square root of the diagonal elements of the covariance matrix for the parameters being fitted; these errors are obtained from the code via the inclusion of an error array, consisting of the measured RMS noise of the data divided by the pixel weights.

As was found by the earlier work of RER98, de Vaucouleurs profiles provide a far better fit to the data than either pure point source or exponential disc models. For those galaxies which overlap with the RER98 sample our own modelling confirms this result, and in general the results of our fitting for a pure de Vaucouleurs profile produce very similar best-fitting effective radii to those of RER98 (with occasional exceptions such as 6C 1129+37 which was not previously known to consist of a pair of elliptical galaxies). However, a more representative model of these galaxies should also include an unresolved nuclear point source contribution. A 'point source fraction' has been included as an additional free parameter in our modelling of these sources, alongside the effective radius, peak intensity, galaxy centroid and ellipticity. One issue with this modelling is the potential degeneracy between the shape of the galaxy profile and the derived nuclear point source contribution: a combination of large $r_{\rm eff}$ and high point source contribution often produces a similar reduced χ^2 value to a smaller galaxy with a much lower point source contribution. This behaviour of the reduced χ^2 for various values of $r_{\rm eff}$ and the point source fraction is clearly illustrated and constrained by the shape of our χ^2 contours in Figs 1–10. We have also considered the slightly more complex Sérsic profile (i.e. $r^{1/n}$ rather than simply $r^{1/4}$; Sérsic 1968) for the single galaxy systems in our sample (i.e. excluding 6C 1100+35, 1129+37 and 1256+36). The Sérsic profile can account for slight variations in the slope of the galaxy profiles compared with the predictions of a de Vaucouleurs model. In particular, a galaxy with a high nuclear point source contribution may in fact be better modelled by a Sérsic profile with $n > 4$, the steeper slope of which incorporates a higher luminosity for the

central regions. We find that for the majority of our sources a value of $n \sim 4$ is preferred (although a few sources are better fit by Sérsic profiles with a higher/lower value of n), confirming that in general the host galaxies are well-behaved elliptical galaxies. However, the uncertainties on the actual slope of the profiles are not insignificant, and the quality of our data is not sufficient for us to accurately constrain the profile shape (i.e. n), size, point source component and other parameters independently. Therefore, for ease of comparison with previous data sets and given that $n \sim 4$ is the preferred value, we restrict our detailed analysis to de Vaucouleurs elliptical profiles with $n = 4$; a brief discussion of the effects of deviations from de Vaucouleurs profiles is included where relevant in Section 2.3.

Tabulated results of our modelling can be found in Table 1, with errors determined as described earlier in this section. Figs 1–10 display the following for each source: the K-band galaxy images (a), best-fitting model (after convolution with the appropriate PSF) (b), the residuals obtained after subtracting this model from the original data (c), a radially averaged 1D profile of these data and best-fitting model (d) and contours representing the reduced χ^2 (ideally $\sim$1 for an accurate fit; actual values for each source listed in Table 1) plus 1, 2, 3, 5 and 10 (e). Examination of the value of χ^2 over the local parameter space provides a further check on the accuracy of our fitting; although these results do not consider the error on the other free parameters, the $\chi^2 + 1$ contours cover a similar range to the 1σ errors on each parameter deduced as part of the fitting process, and provide a valuable visualization of the accuracy of our modelling.

As a final test of the accuracy of the fitting procedures, the parameters of the best-fitting models were used to construct artificial galaxies. After adding noise to the data so as to reproduce the S/N ratio of the original observations, the same routines were used to fit the parameters of the artificial data. In this way, we have been able to investigate the tendency of the routine to over- or underestimate the value of a given parameter for a particular source, and the range of data which provide consistent results (i.e. which produce artificial galaxies indistinguishable from the actual object). The range of values given for errors on $r_{\rm eff}$, ϵ and the point source fraction in Table 1 agree well with the range of input data which gave results consistent with the observations.

2.2 Rest-frame UV morphologies

We have repeated the fitting process for our WFPC2 *HST* observations of a number of 6C sources (see Paper I for details), excluding those with the most complicated UV morphologies (6C 1129+37) and lowest S/N ratio (6C 0825+34). PSFs were determined using two methods: first by extracting the profiles of unsaturated stellar objects on the WF3 fields; and secondly via the TINYTIM software. No significant differences were observed between the data PSFs and the TINYTIM PSFs; the latter were used for this analysis.

For the remaining galaxies, we have masked out the regions of the image which contain the aligned emission. However, this is only practical for emission which is well separated from the host galaxy. Any remaining aligned emission, particularly within the central few arcsec, may potentially skew the fit. For most sources we do obtain good 2D fits. But for some others, in spite the high resolution of the *HST* data, accurate fitting becomes impossible; this is generally owing to the presence of either dust lanes, bright aligned/excess UV emission coincident with the host galaxy, or the low S/N ratio of the underlying galaxy. In these cases the K-band fits are used to fix the characteristic radius; this allows the best-fitting nuclear point source contribution to be determined, and also permits a clear examination of the excess UV emission. The resulting models/residuals

---

[1] A non-linear least-squares curve fitting package available via http://astrog.physics.wisc.edu/~craigm/idl/fitting.html developed by Craig Markwardt.
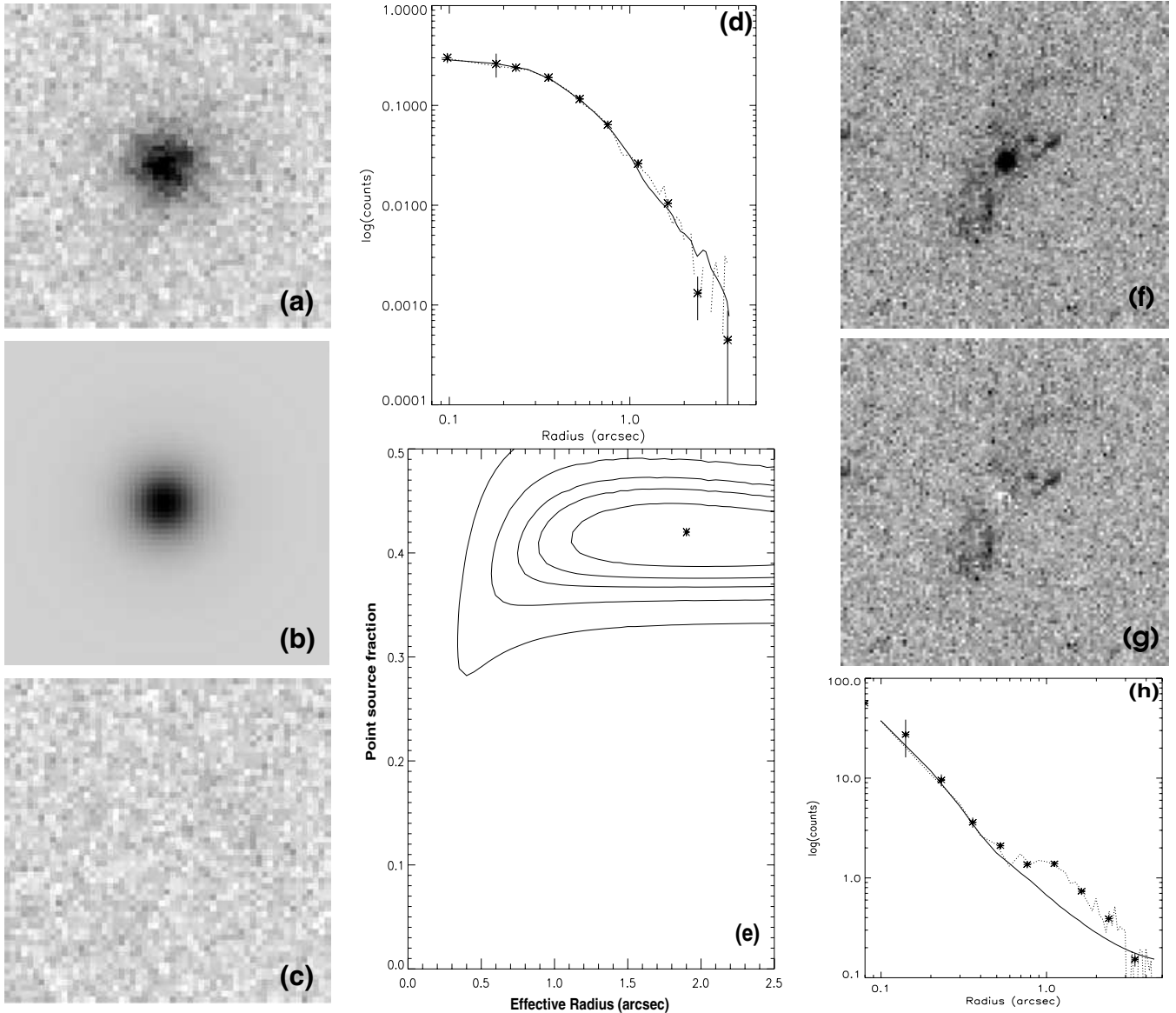
Figure 1. Host galaxy morphology fits for the galaxy 6C 0943+39. The *K*-band galaxy image is presented in frame (a), with the model galaxy given in frame (b) and the residuals after subtracting the best-fitting model from the data displayed in frame (c). Frame (d) illustrates a 1-dimensional (1D) profile of these data (dotted line and binned points) with the best-fitting model (solid line) overlaid. Frame (e) displays the minimum reduced χ^2 (marked with a cross), plus contours for $\chi^2_{min} + 1$, $\chi^2_{min} + 2$, $\chi^2_{min} + 3$, $\chi^2_{min} + 5$ and $\chi^2_{min} + 10$. The variation in χ^2 was determined by fitting the galaxy whilst fixing the values of r_{eff} and the point source fraction at increments of 0.05 arcsec and 1 per cent of the total flux respectively; other parameters (galaxy peak intensity and centroid) were free to vary. For models with a point source fraction of 0.0 per cent, the minimum value of χ^2 lies at $r_{eff} \sim 0.15$ arcsec. Frame (f) displays the *HST* data for this source. The residual flux after subtraction of the best-fitting model galaxy is displayed in frame (g) and frame (h) illustrates a 1D profile of these data (dotted line and binned points) with the best-fitting model (solid line).

produced by this analysis are displayed in Figs 1–10, and the overall fit parameters are given in Table 1.

One potential pitfall of this approach is that the observed effective radii of such galaxies may vary with wavelength. The host galaxies of powerful radio sources typically display bluer colours than those of other elliptical galaxies; in addition to the obvious effects of a nuclear point source or the alignment effect, excess blue emission may be spatially extended throughout the galaxy (e.g. Smith & Heckman 1989; Govoni et al. 2000). There is also some evidence that powerful radio galaxies become bluer towards their centres, contrary to the behaviour of normal elliptical galaxies (Mahabal, Kembhavi & McCarthy 1999). If this is the case, the effective radii

of the galaxies modelled in the rest-frame UV would be smaller than those measured using our longer wavelength *K*-band observations, and the resulting nuclear point source contributions could have been overestimated.

2.3 Notes on individual sources

6C 0825+34

6C 0825+34, at a redshift of $z = 1.47$, is the most distant source of the sample. The S/N level for this source is the lowest in the sample, and fitting a simple de Vaucouleurs profile suggests an effective
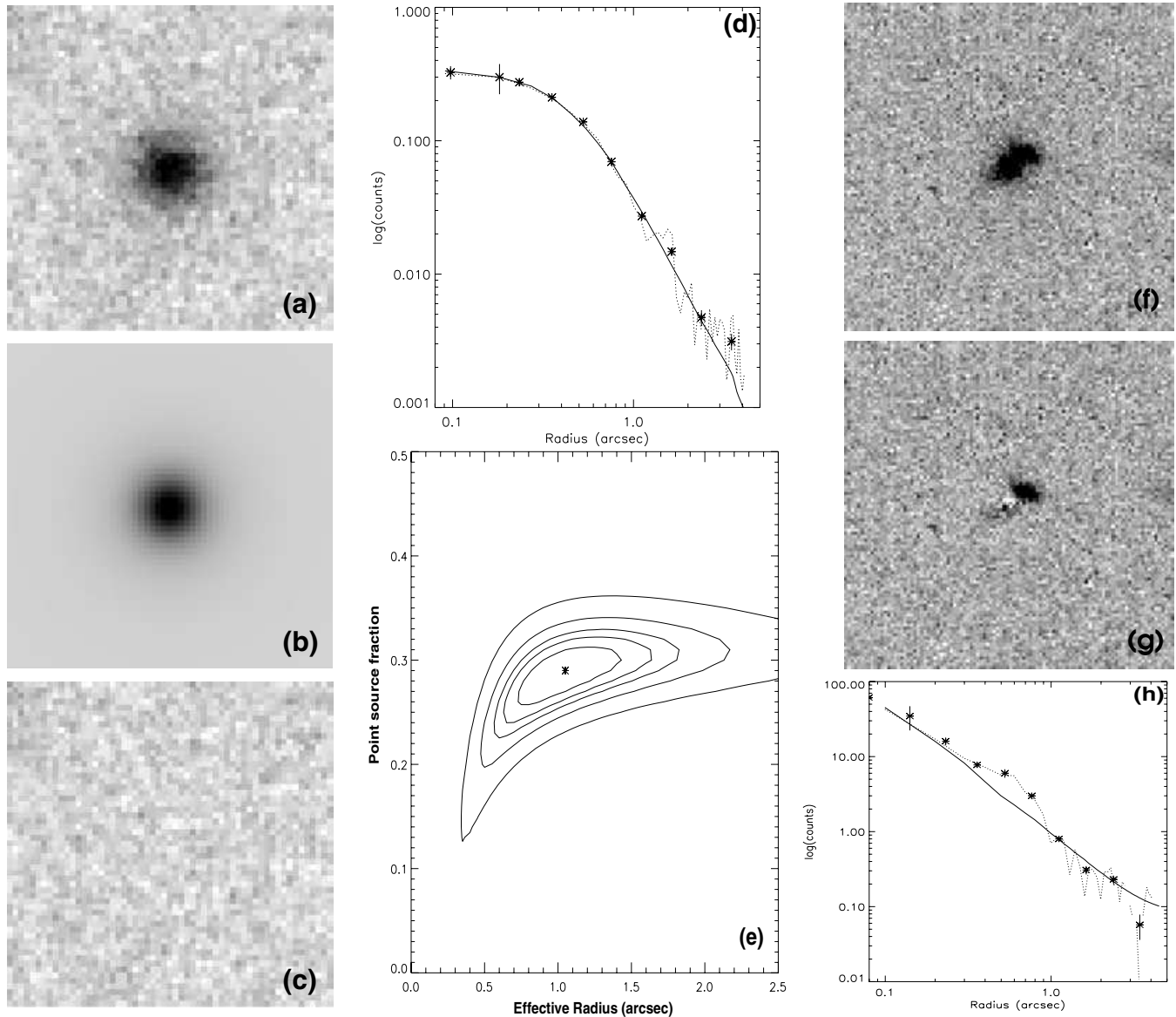
Figure 2. Host galaxy morphology fits for the galaxy 6C 1011+36. The *K*-band galaxy image is presented in frame (a), with the model galaxy given in frame (b) and the residuals after subtracting the best-fitting model from the data displayed in frame (c). Frame (d) illustrates a 1D profile of these data (dotted line and binned points) with the best-fitting model (solid line) overlaid. Frame (e) displays the minimum reduced χ^2 (marked with a cross), plus contours for $\chi^2_{\min} + 1$, $\chi^2_{\min} + 2$, $\chi^2_{\min} + 3$, $\chi^2_{\min} + 5$ and $\chi^2_{\min} + 10$. For models with a point source fraction of 0.0 per cent, the minimum value of χ^2 lies at $r_{\mathrm{eff}} \sim 0.25$ arcsec. Frame (f) displays the *HST* data for this source. The residual flux after subtraction of the best-fitting model galaxy is displayed in frame (g), and frame (h) illustrates a 1D profile of these data (dotted line and binned points) with the best-fitting model (solid line).

radius of 0.2 ± 0.05 arcsec. However, if we also allow the inclusion of a nuclear point source contribution, neither the effective radius nor the point source fraction can be accurately constrained. The rest-frame UV image of this galaxy (which shows a small, faint galaxy with a secondary emission peak aligned with the radio source axis; Paper I) does not provide much help in accurately constraining the structural parameters of this object.

6C 0943+39

Fitting this galaxy solely with a simple de Vaucouleurs elliptical galaxy profile results in a best-fitting effective radius of 0.15 arcsec, which is in good agreement with the value of $r_{\mathrm{eff}} = 0.27^{+0.33}_{-0.14}$ arcsec given by the previous fitting of RER98. However, the data greatly favour a fit including a nuclear point source contribution; the best-

fitting values being an effective radius of 1.9 ± 0.4 arcsec and a point source percentage of 41.5 per cent. Profile fitting of the WFPC2 observations of this source is not possible, owing to the extensive aligned emission surrounding this source. However, fitting using the best-fitting value of r_{eff} already obtained from our IR data suggests a point source contribution in the F702W filter of 36 per cent; the subtraction of this model galaxy and point source does not leave any obvious residual features other than the aligned emission already apparent in the images (Table 1; Fig. 1).

6C 1011+36

Once again, although the fit obtained with a pure de Vaucouleurs profile ($r_{\mathrm{eff}} = 0.25$ arcsec) was in good agreement with the RER98 result ($r_{\mathrm{eff}} = 0.19^{+0.09}_{-0.11}$ arcsec), the best fit for 6C 1011+36 also
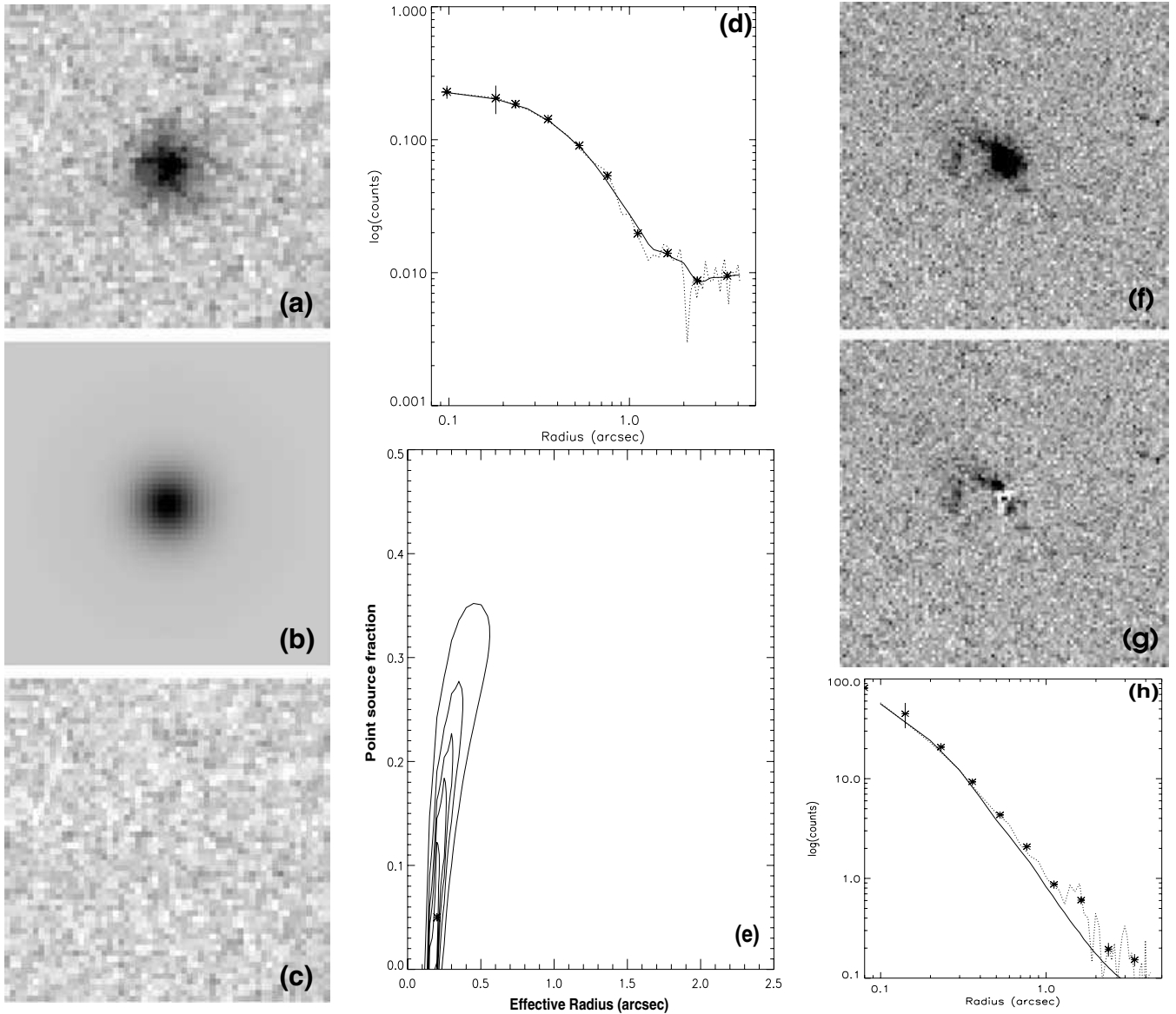
Figure 3. Host galaxy morphology fits for the galaxy 6C 1017+37. The *K*-band galaxy image is presented in frame (a), with the model galaxy given in frame (b) and the residuals after subtracting the best-fitting model from the data displayed in frame (c). Frame (d) illustrates a 1D profile of these data (dotted line and binned points) with the best-fitting model (solid line) overlaid. Frame (e) displays the minimum reduced χ^2 (marked with a cross), plus contours for $\chi^2_{min} + 1$, $\chi^2_{min} + 2$, $\chi^2_{min} + 3$, $\chi^2_{min} + 5$ and $\chi^2_{min} + 10$. Frame (f) displays the *HST* data for this source. The residual flux after subtraction of the best-fitting model galaxy is displayed in frame (g), and frame (h) illustrates a 1D profile of these data (dotted line and binned points) with the best-fitting model (solid line).

consists of a combination of point source (28.8 per cent) and elliptical galaxy ($r_{eff} = 1.0$ arcsec). The aligned emission surrounding this source is particularly luminous and difficult to completely mask, rendering a fit of the rest-frame UV morphology impractical. Using the *K*-band effective radius suggests a point source contribution of 25 per cent. After subtraction of the model galaxy, both the luminous aligned emission to the north-west of the galaxy and fainter emission to the south are clearly visible in the residual image (Fig. 2).

6C 1017+37

This galaxy was relatively easy to fit, and our resulting value of $r_{eff} = 0.2$ arcsec is again in close agreement with the RER98 value ($r_{eff} = 0.12^{+0.19}_{-0.06}$ arcsec). We have also carried out profile fitting of the WFPC2 observations of this source, masking out the aligned

emission as well as possible. The resulting fit is in good agreement with that of our IR data, giving an effective radius of 0.28 arcsec and a point source contribution of 12 per cent. However, we believe this larger size may reflect incomplete masking of aligned emission very close to the host galaxy. Fixing the effective radius at $r_{eff} = 0.2$ arcsec suggests a slightly lower point source contribution of 9 per cent; the full structure of the aligned emission is clearly visible in the residual image (Fig. 3).

6C 1019+39

In addition to lying at the lowest redshift in the sample ($z = 0.922$), the UKIRT and *HST* images of 6C 1019+39 show it to have the most noticeable ellipticity of the galaxies in this sample. Fitting the *K*-band data clearly rules out any significant point source
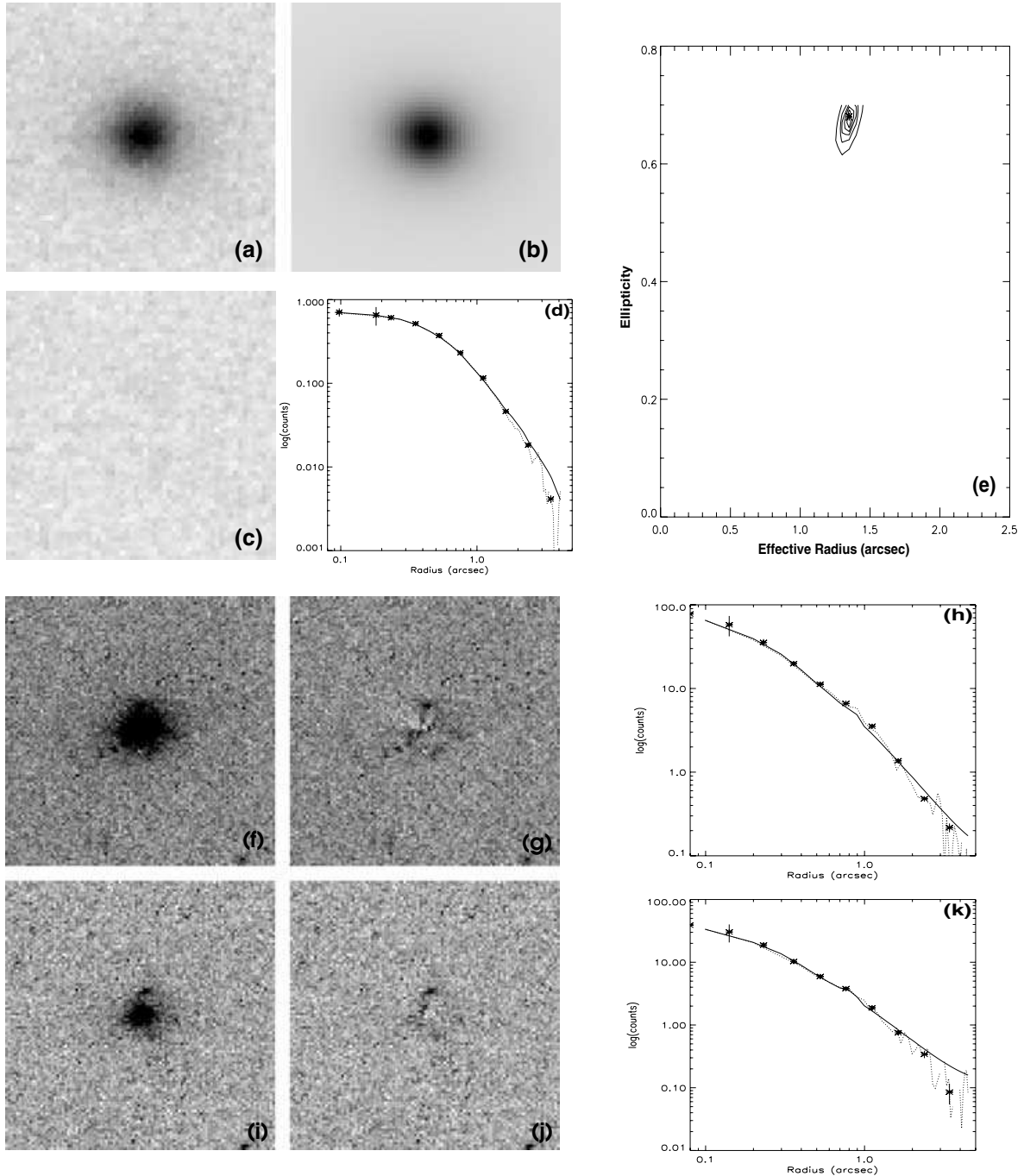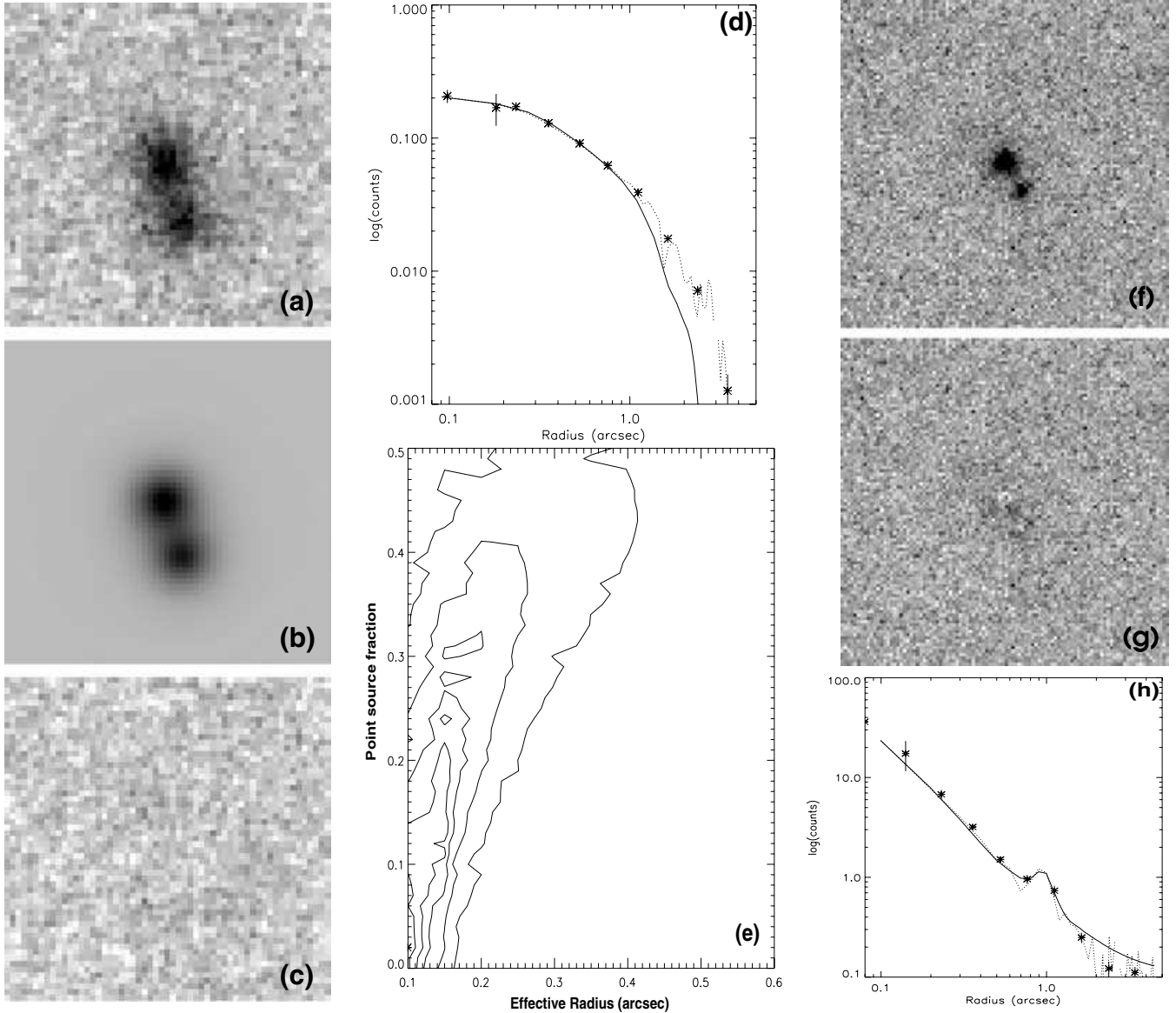
Figure 4. Host galaxy morphology fits for the galaxy 6C 1019+39. The *K*-band galaxy image is presented in frame (a), with the model galaxy given in frame (b) and the residuals after subtracting the best-fitting model from the data displayed in frame (c). Frame (d) illustrates a 1D cut through the data (dotted line and binned points) with the best-fitting model (solid line) overlaid. Frame (e) displays the minimum reduced χ^2 (marked with a cross), plus contours for $\chi^2_{min} + 1$, $\chi^2_{min} + 2$, $\chi^2_{min} + 3$, $\chi^2_{min} + 5$ and $\chi^2_{min} + 10$. The variation in χ^2 (frame e) was determined by fitting the galaxy whilst fixing the values of r_{eff}, galaxy ellipticity (ϵ) and the point source fraction at increments of 0.05 arcsec, 0.01 and 1 per cent of the total flux respectively; other parameters (galaxy peak intensity and centroid) were free to vary. As $\epsilon \rightarrow 0.0$, $r_{eff} \rightarrow 1.0$ arcsec. The point source fraction giving the minimum χ^2 remains at 0 ± 1 per cent for all preferred values of r_{eff} and ϵ. Frame (f) displays the *HST* data for this source in the F814W filter. The residual flux after subtraction of the best-fitting model galaxy is displayed in frame (g), and frame (h) illustrates a 1D profile of these data (dotted line and binned points) with the best-fitting model (solid line). The same data for the F606W filter are displayed in frames (i), (j) and (k).

contribution, but also suggests a rather large ellipticity of 0.69, and an effective radius of 1.18 arcsec along the major axis. (However, we see little change if we fit over a range of ϵ: the effective radius converges to a minimum value of 1.0 arcsec as $\epsilon \rightarrow 0$ and the model

galaxy becomes spherical.) Similar results are obtained for all three parameters using the *HST* data, which suggest effective radii of 1.16 and 1.04 arcsec for the F606W and F814W filters, respectively. The residual image also allows us to see several faint clumps of excess

Figure 5. Host galaxy morphology fits for the galaxy 6C 1100+35. The *K*-band galaxy image is presented in frame (a), with the model galaxy given in frame (b) and the residuals after subtracting the best-fitting model from the data displayed in frame (c). Frame (d) illustrates a 1D cut through the data (dotted line and binned points) with the best-fitting model (solid line) overlaid. Frame (e) displays the minimum reduced χ^2 (marked with a cross), plus contours for $\chi^2_{min} + 1$, $\chi^2_{min} + 2$, $\chi^2_{min} + 3$, $\chi^2_{min} + 5$ and $\chi^2_{min} + 10$. Owing to the increases in time required for fitting multiple sources, the variation in χ^2 was initially determined at low resolution over the same range of parameters as for other sources, prior to being repeated over a reduced range of values for r_{eff}. Values of r_{eff} and the point source fraction were incremented by 0.05 arcsec and 1 per cent of the total flux respectively whilst other parameters (galaxy peak intensity and centroid, second galaxy parameters) were free to vary (within sensible limits in the case of the companion object). Frame (f) displays the *HST* data for this source. The residual flux after subtraction of the best-fitting model galaxy is displayed in frame (g), and frame (h) illustrates a 1D profile of these data (dotted line and binned points) with the best-fitting model (solid line).

UV emission surrounding this galaxy; although this source displays very little aligned emission, it does possess very luminous line emission likely triggered by a combination of both AGN photoionization and shocks associated with the radio source (Inskip et al. 2002b).

6C 1100+35

Along with 6C 0825+34 and 1204+35, this source is one of the three higher redshift sources in the sample. Owing to the unusually strong radio emission along the jet axis on one side of this source, it is

plausible that this source may be orientated closer to the line of sight than the average for this sample, and a high point source contribution would therefore not be unexpected. Owing to the close proximity of a second object, we fit both objects together. The resulting best fit suggests a galaxy with 0.16 arcsec with a point source contribution of 15 ± 14 per cent.

As this source displays no obvious aligned emission, it is also useful to repeat the fitting process for the *HST* data. However, given the strong point source contribution to 6C 1100+35 in the rest-frame UV and the relatively small sizes of both sources, we unfortunately find that the effective radius and point source contribution become
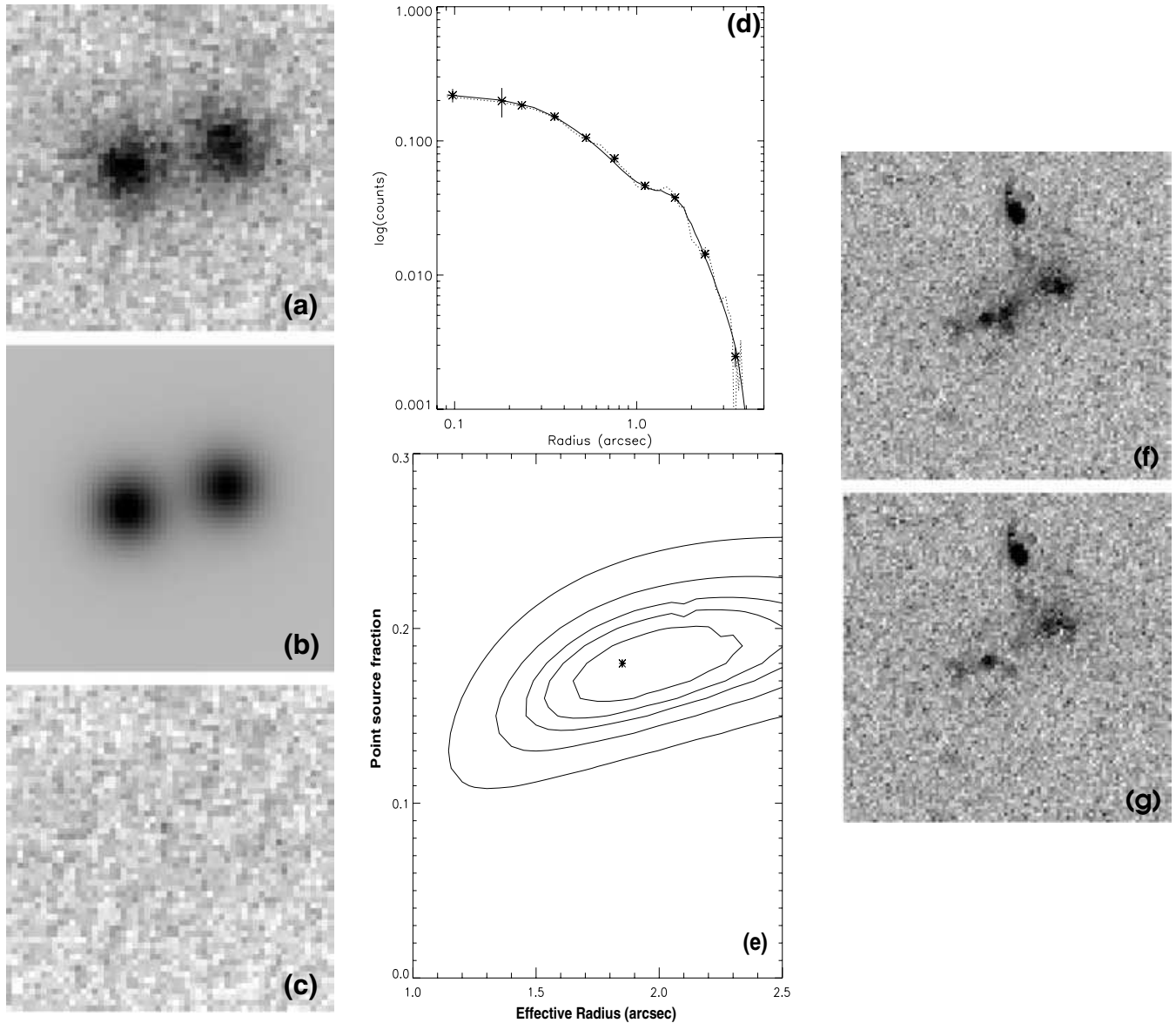
Figure 6. Host galaxy morphology fits for the galaxy 6C 1129+37. The *K*-band galaxy image is presented in frame (a), with the model galaxy given in frame (b) and the residuals after subtracting the best-fitting model from the data displayed in frame (c). Frame (d) illustrates a 1D cut through the data (dotted line and binned points) with the best-fitting model (solid line) overlaid. Frame (e) displays the minimum reduced χ^2 (marked with a cross), plus contours for $\chi^2_{min} + 1$, $\chi^2_{min} + 2$, $\chi^2_{min} + 3$, $\chi^2_{min} + 5$ and $\chi^2_{min} + 10$. Owing to the increases in time required for fitting multiple sources, the variation in χ^2 was initially determined at low resolution over the same range of parameters as for other sources, prior to being repeated over a reduced range of values for r_{eff}. Values of r_{eff} and the point source fraction were incremented by 0.05 arcsec and 1 per cent of the total flux respectively whilst other parameters (galaxy peak intensity and centroid, second galaxy parameters) were free to vary (within sensible limits in the case of the companion object). Frame (f) displays the *HST* data for this source. The residual flux after subtraction of the best-fitting model galaxy is displayed in frame (g).

considerably degenerate. Using the best-fitting results obtained from our *K*-band observations gives a maximum point source contribution in the F814W filter of 41 per cent.

6C 1129+37

Our *K*-band image of this source clearly reveals a pair of elliptical galaxies, of roughly similar luminosity. As was the case for 6C 1100+35, these two galaxies need to be fitted simultaneously, giving a best-fitting value of 1.8 arcsec for the radio galaxy and a point source contribution of 18 per cent. Owing to the extreme aligned

emission surrounding this source in the rest-frame UV, accurate fitting of our *HST* data is not possible. We have, however, attempted the removal of the host galaxy assuming the *K*-band effective radius and zero-point source, to permit examination of the remaining aligned emission (Fig. 6g).

6C 1204+35

For this source, we find best-fitting values of $r_{eff} = 0.85$ arcsec and a point source fraction of 13 per cent (our results for a pure de Vaucouleurs profile with zero-point source are again in good
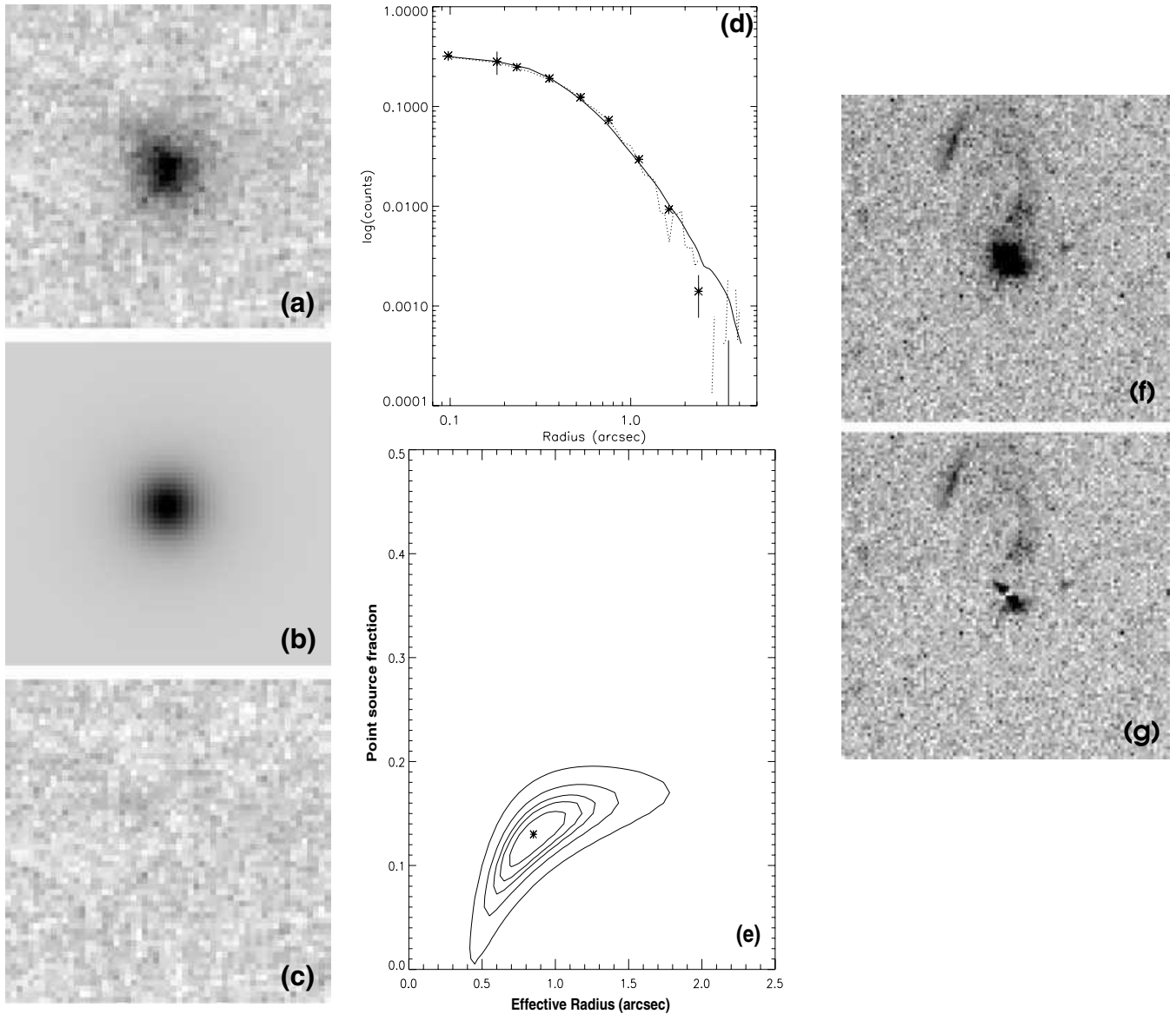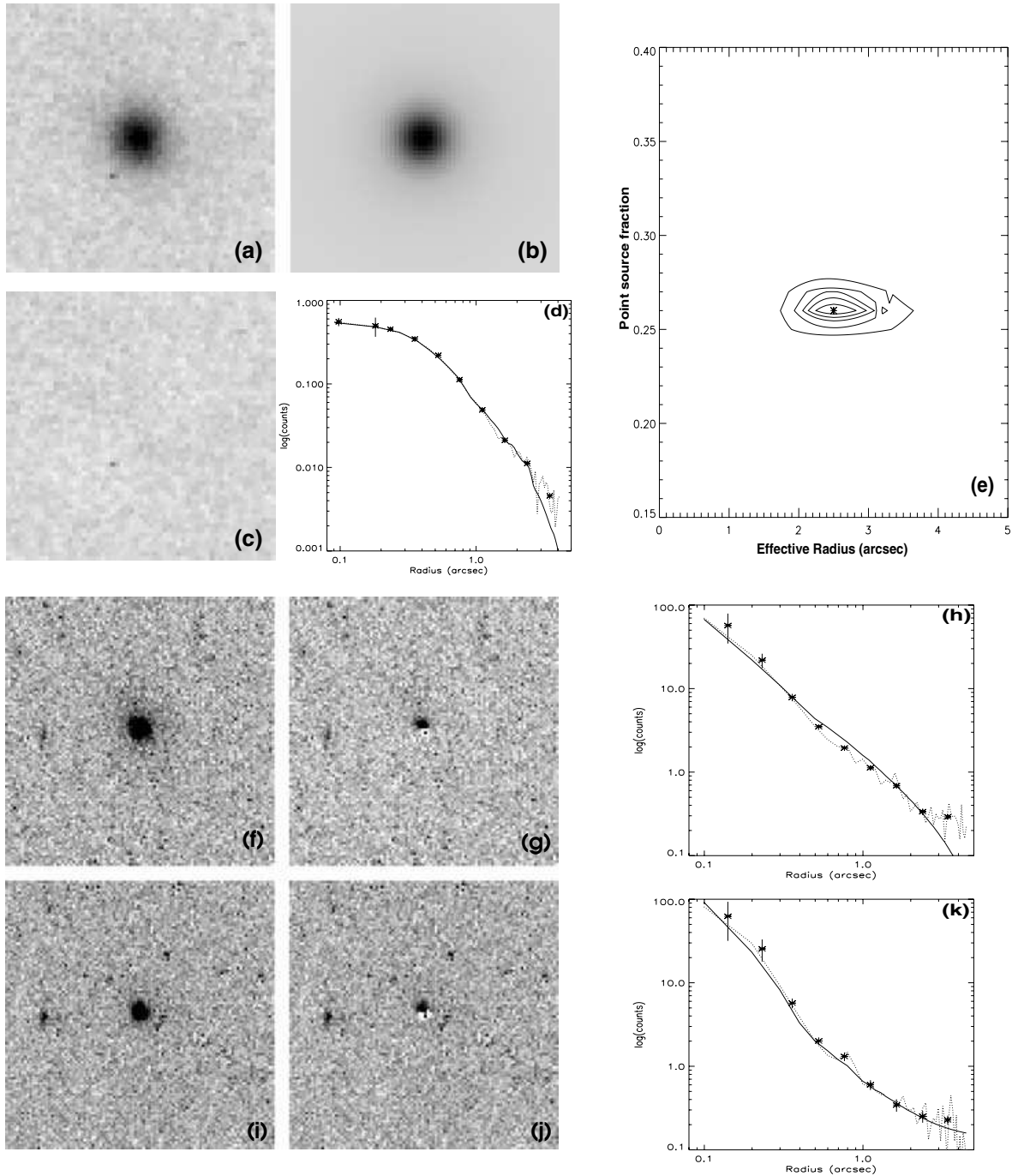
Figure 7. Host galaxy morphology fits for the galaxy 6C 1204+35. The *K*-band galaxy image is presented in frame (a), with the model galaxy given in frame (b) and the residuals after subtracting the best-fitting model from the data displayed in frame (c). Frame (d) illustrates a 1D cut through the data (dotted line and binned points) with the best-fit model (solid line) overlaid. Frame (e) displays the minimum reduced χ^2 (marked with a cross), plus contours for $\chi^2_{min} + 1$, $\chi^2_{min} + 2$, $\chi^2_{min} + 3$, $\chi^2_{min} + 5$ and $\chi^2_{min} + 10$. For models with a point source fraction of 0.0 per cent, the minimum value of χ^2 lies at $r_{eff} \sim 0.45$ arcsec. Frame (f) displays the *HST* data for this source. The residual flux after subtraction of the best-fitting model galaxy is displayed in frame (g).

agreement with the RER98 results, 0.45 arcsec cf. $0.51^{+0.10}_{-0.14}$ arcsec). The WFPC2 observations of 6C 1204+35 cannot be easily fitted. Fig. 7 displays the residuals produced after fitting this galaxy with the best-fitting effective radius found for the IR data. These clearly show that there is either a dust lane/disc lying across the galaxy perpendicular to the radio axis, or (perhaps less likely) bright aligned emission lying along the radio axis through the centre of the galaxy. Interestingly, Sérsic profile fitting of the *K*-band observations of this system imply values of $n \sim 2$, $r_{eff} = 0.73$ arcsec and a higher point source contribution of 22 per cent. This suggests that although the nuclear emission is strong, the emission in the inner ($r < r_{eff}$) regions of the host galaxy has a shallower profile than a de Vaucouleurs elliptical, perhaps owing in part to dust extinction.

6C 1217+36

Once again, although our pure de Vaucouleurs profile fit ($r_{eff} = 0.55$ arcsec) is in good agreement with the RER98 fit ($0.44^{+0.18}_{-0.20}$ arcsec), the data very much favour an additional point source contribution, giving best-fitting values of $r_{eff} = 2.5$ arcsec and 25 per cent. Sérsic profile fitting of this source predicts $n = 5.4$, a similar point source contribution of 22 per cent and a somewhat larger $r_{eff} = 3.9$ arcsec. We also expect a high point source contribution in our *HST* images, based on the very blue colours of this source coupled with the lack of any large-scale aligned emission. Point source contribution and effective radius again prove difficult to disentangle from our *HST* images. Given the excess emission visible in the residual image (offset slightly to the north from the
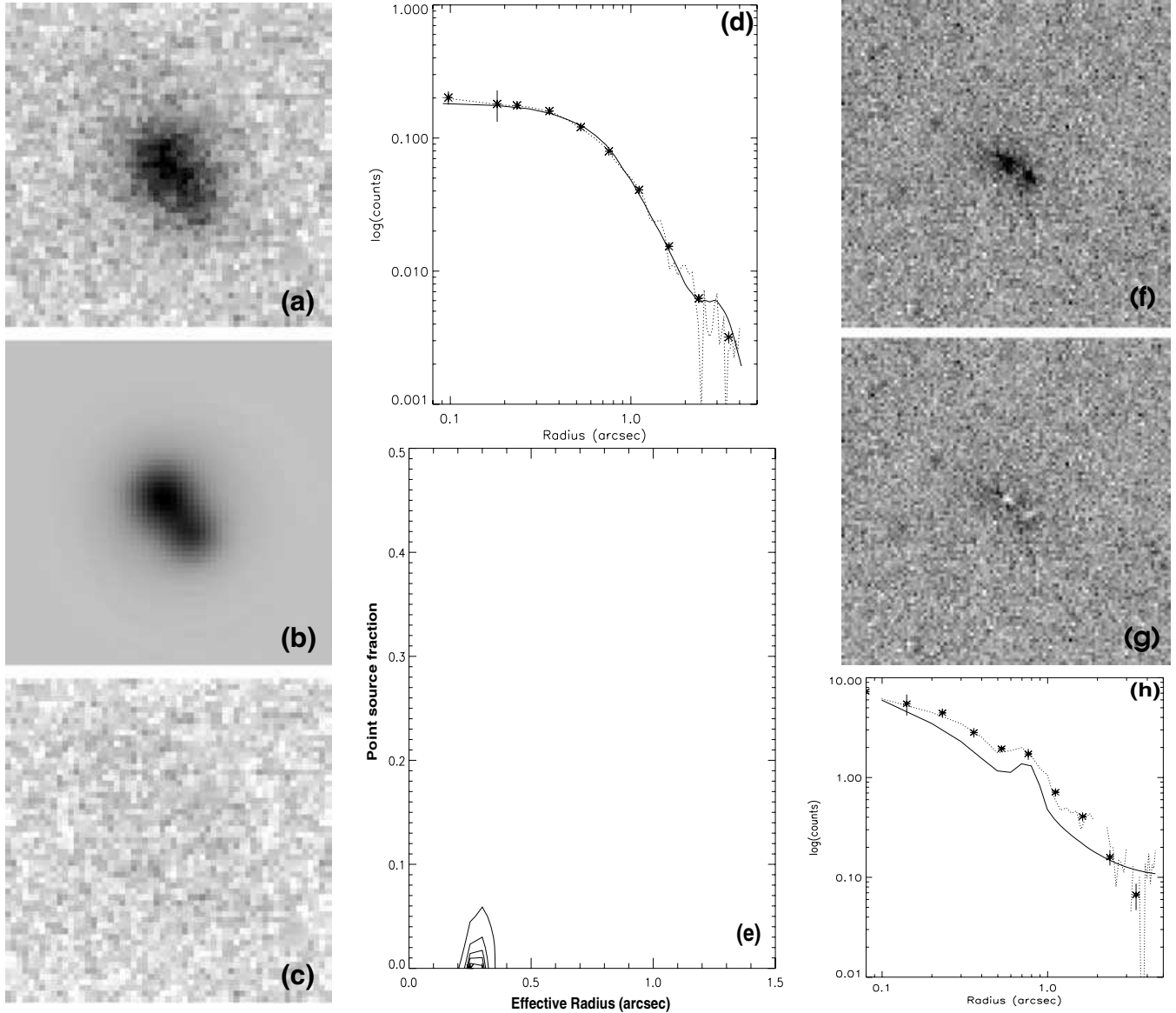
Figure 8. Host galaxy morphology fits for the galaxy 6C 1217+36. The *K*-band galaxy image is presented in frame (a), with the model galaxy given in frame (b) and the residuals after subtracting the best-fitting model from the data displayed in frame (c). Frame (d) illustrates a 1D cut through the data (dotted line and binned points) with the best-fitting model (solid line) overlaid. Frame (e) displays the minimum reduced χ^2 (marked with a cross), plus contours for $\chi^2_{min} + 1$, $\chi^2_{min} + 2$, $\chi^2_{min} + 3$, $\chi^2_{min} + 5$ and $\chi^2_{min} + 10$. For models with a point source fraction of 0.0 per cent (very unlikely for this particular source), the minimum value of χ^2 lies at $r_{eff} \sim 0.55$ arcsec. Frame (f) displays the *HST* data for this source in the F814W filter. The residual flux after subtraction of the best-fitting model galaxy is displayed in frame (g), and frame (h) illustrates a 1D profile of these data (dotted line and binned points) with the best-fitting model (solid line). The same data for the F606W filter are displayed in frames (i), (j) and (k).

centre of the galaxy), and the low S/N ratio of the underlying host galaxy, this is hardly surprising.

6C 1256+36

This source displays the most elongated *K*-band morphology; the major question for this source is whether this elongation is owing

to a strong *K*-band alignment effect (such as that seen for some sources in the more powerful 3CR subsample of Best et al. 1997), the natural elongation of the elliptical host galaxy, a close pair of galaxies, or a single galaxy combined with an unresolved point source. Single object fits could not provide an adequate fit to the data, but much better fits were obtained fitting two objects simultaneously. The positions of the two components in the *K*-band are
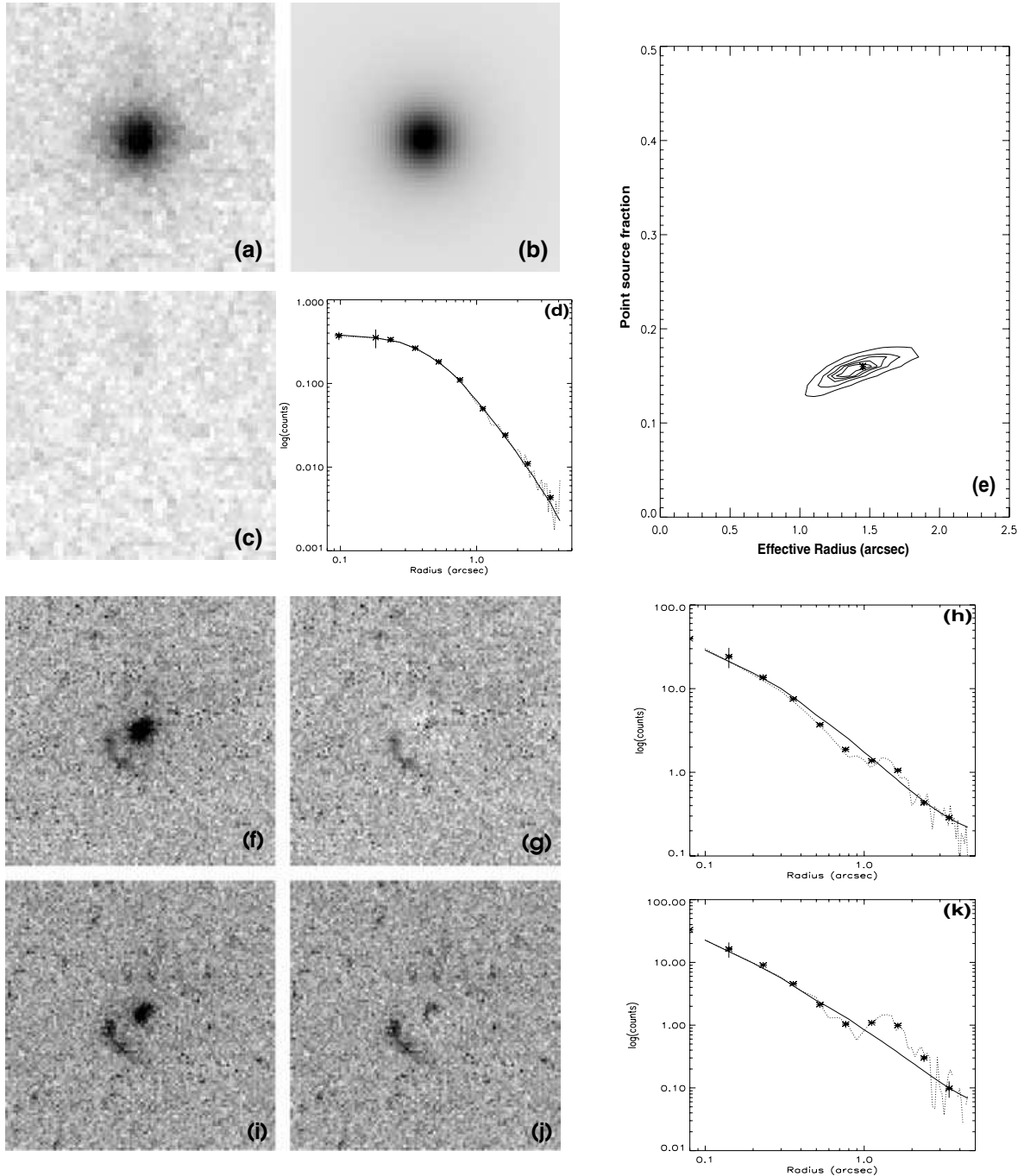
Figure 9. Host galaxy morphology fits for the galaxy 6C 1204+35. The fitting of this source also included the presence of an unresolved companion object, the flux and position of which were additional free parameters. The *K*-band galaxy image is presented in frame (a), with the model galaxy given in frame (b) and the residuals after subtracting the best-fitting model from the data displayed in frame (c). Frame (d) illustrates a 1D cut through the data (dotted line and binned points) with the best-fit model (solid line) overlaid. Frame (e) displays the minimum reduced χ^2 (marked with a cross), plus contours for $\chi^2_{min} + 1$, $\chi^2_{min} + 2$, $\chi^2_{min} + 3$, $\chi^2_{min} + 5$ and $\chi^2_{min} + 10$. Frame (f) displays the *HST* data for this source. The residual flux after subtraction of the best-fitting model galaxy is displayed in frame (g), and frame (h) illustrates a 1D profile of these data (dotted line and binned points) with the best-fitting model (solid line).

coincident with the two peaks visible in our *HST* image. Whilst fitting this source, the positions of both objects were free parameters, as were their effective radii and fractional point source contributions. The best fits were obtained for an unresolved 'companion' object, hardly surprising given its point-like appearance on the *HST* image. Overall, this stellar object has a flux equivalent to roughly 34 per cent of the total *K*-band flux from this galaxy (i.e. a 25 per cent contribution to the aperture flux for this object). Whilst the point-like nature of the adjacent object (hereafter assumed to be a foreground star) is clear from the WFPC2 observations of this source, the host galaxy itself is relatively faint and is not well suited to profile fitting. Fitting using the best-fitting parameters of the IR imaging produces negligible residuals; in this case the flux of the adjacent object accounts for 17 per cent of the total flux in the

aperture (i.e. equivalent to 20 per cent of the flux from the galaxy itself).

6C 1257+36

As is the case for the majority of our objects the best fit for this object consists of a combination of elliptical galaxy ($r_{eff} = 1.39$ arcsec) and nuclear point source (16 per cent); if we exclude the point source contribution (which clearly gives a much worse fit than the models including a point source) the suggested effective radius (0.55 arcsec) is similar to (although somewhat higher than) the RER98 value ($0.37^{+0.07}_{-0.08}$ arcsec). Fitting this system with a Sérsic profile suggests values of $n = 6.1$, $r_{eff} = 1.8$ arcsec and a point source contribution of 12 per cent. The presence of excess UV emission to the north

Figure 10. Host galaxy morphology fits for the galaxy 6C 1257+36. The *K*-band galaxy image is presented in frame (a), with the model galaxy given in frame (b) and the residuals after subtracting the best-fitting model from the data displayed in frame (c). Frame (d) illustrates a 1D cut through the data (dotted line and binned points) with the best-fit model (solid line) overlaid. Frame (e) displays the minimum reduced χ^2 (marked with a cross), plus contours for $\chi^2_{\min} + 1$, $\chi^2_{\min} + 2$, $\chi^2_{\min} + 3$, $\chi^2_{\min} + 5$ and $\chi^2_{\min} + 10$. For models with a point source fraction of 0.0 per cent, the minimum value of χ^2 lies at $r_{\rm eff} \sim$ 0.55 arcsec. Frame (f) displays the *HST* data for this source in the F814W filter. The residual flux after subtraction of the best-fitting model galaxy is displayed in frame (g), and frame (h) illustrates a 1D profile of these data (dotted line and binned points) with the best-fitting model (solid line). The same data for the F606W filter are displayed in frames (i), (j) and (k).

of the galaxy (as well as to the east, as can be seen in the residual images: Fig. 10) makes fitting the *HST* images less straightforward; with the exception of these features, the effective radius implied by the *K*-band fitting seems to provide a reasonable fit, suggesting point source contributions of 11 per cent in the F606W filter, and 3.5 per cent in the F814W filter.

2.4 Comparison with other radio source samples

Analysis of the radio galaxy *K*–*z* relation (Inskip et al. 2002a) shows that whilst the 6C and 3CR galaxy populations are indistinguishable at low redshifts, the two populations differ in their mean magnitude by approximately $K \sim 0.6$ mag at higher redshifts. If galaxy

Table 1. Results of galaxy surface profile fitting. Source name and redshift are listed in columns 1 and 2. The filter used for each observation is listed in column 3. The best-fitting effective radius for each source is given in columns 4 (arcsec) and 5 (kpc), with the best-fitting nuclear point source contribution listed in column 6. Column 7 gives the value of the reduced χ^2 for the fit.

(1) Source	(2) Redshift	(3) Filter	(4) $r_{\rm eff}$ (arcsec)	(5) $r_{\rm eff}$ (kpc)	(6) Point source fraction (per cent)	(7) Reduced χ^2
6C 0825+34	1.467	K	S/N ratio too low for accurate fitting[a]			–
		F814W	–	–	–	–
6C 0943+39	1.035	K	1.90 ± 0.40	16.5 ± 3.5	41.5 ± 3.5	0.98
		F702W	1.9^b	16.5^b	36^{+6}_{-4}	1.16
6C 1011+36	1.042	K	$1.00^{+0.19}_{-0.09}$	$8.7^{-1.7}_{+0.8}$	28.8 ± 1.0	1.10
		F702W	1.04 ± 0.05	9.0 ± 0.4	25 ± 2	1.27
6C 1017+37	1.053	K	0.20 ± 0.05	1.7 ± 0.4	4^{+13}_{-4}	1.09
		F702W	0.28 ± 0.1	2.4 ± 0.9	12 ± 3	2.17
6C 1019+39[c]	0.922	K	1.18 ± 0.01	10.0 ± 0.1	0.0 ± 1.0	1.25
		F814W	1.04 ± 0.06	8.8 ± 0.5	0 ± 1	1.29
		F606W	1.16 ± 0.2	9.8 ± 1.7	0 ± 2	1.20
6C 1100+35	1.440	K	0.16 ± 0.04	1.5 ± 0.4	15 ± 14	1.49
		F814W	0.2 ± 0.1	1.9 ± 0.9	41^{+11}_{-1}	1.16
6C 1129+37 (radio galaxy)	1.060	K	1.8 ± 0.2	15.7 ± 1.7	18.0 ± 1.0	0.97
(companion galaxy)		K	1.7 ± 0.2	14.9 ± 1.7	14.0 ± 1.0	–
(both galaxies)		F702W	UV morphology too complex for galaxy fitting.			–
6C 1204+35	1.376	K	0.85 ± 0.10	7.7 ± 0.9	13.0 ± 1.0	1.00
		F814W	Strong dust lane prevents accurate fitting of galaxy.			–
6C 1217+36	1.088	K	2.50 ± 0.15	22.0 ± 1.3	25.0 ± 0.5	1.32
		F814W	2.5^d	22.0^d	23 ± 5	1.07
		F606W	2.5^d	22.0^d	$>65^e$	–
6C 1256+36 (radio galaxy)	1.128	K	0.95 ± 0.20	8.4 ± 1.8	0.0 ± 3.0	1.17
(unresolved companion)[f]		K	Accounts for 25 per cent of aperture flux; i.e. 34 per cent of radio galaxy flux.			–
(radio galaxy)[g]		F702W	0.95	8.4	0	1.21
(Unresolved Companion)		F702W	Accounts for 17 per cent of aperture flux; i.e. 20 per cent of radio galaxy flux.			–
6C 1257+36	1.004	K	1.39 ± 0.07	12.0 ± 0.6	16.0 ± 0.5	1.32
		F814W	$1.39^{+0.05}_{-0.7}$ arcsec[h]	$12.0^{+0.4h}_{-6.0}$	$3.5^{+1}_{-3.5}$	1.29
		F606W	$1.39^{+0.3h}_{-0.7}$	$12.0^{+2.6h}_{-6.0}$	11 ± 3	1.18

Notes. [a]Fitting 6C 0825+34 with a pure de Vaucouleurs profile (zero-point source contribution) suggests a best-fitting value of $r_{\rm eff} = 0.2$ arcsec. Fitting more complex profiles are fully degenerate; neither $r_{\rm eff}$ nor the point source contribution can be constrained.

[b]Owing to the extensive aligned emission surrounding 6C 0943+39, the effective radius of this galaxy could not be constrained for the F702W filter. The value obtained from our K-band observations is assumed in order to determine the point source contribution in this waveband. The 1σ uncertainties on the K-band effective radius have been used to help constrain the errors on the point source contribution in the F702W emission.

[c]6C 1019+39 is the only source which has a significant ellipticity. The best-fitting value in the K-band is $\epsilon = 0.69$; but the effective radius of the model galaxy varies very little with ϵ. As $\epsilon \to 0$, $r_{\rm eff}({\rm min}) \to 1.0$ arcsec. The ellipticity obtained from the *HST* images is very similar.

[d]6C 1217+36 has a strong nuclear point source contribution in both *HST* filters. Additionally, there is excess UV flux present offset slightly to the NE from the centre of the host galaxy, and/or a dust lane. Owing to these complicating factors, the effective radius cannot be constrained in the *HST* filters.

[e]The quoted point source contribution for 6C 1217+36 in the F606W filter is the minimum value, giving $\chi^2 \sim 6$.

[f]Unresolved point source offset from host galaxy, possibly a foreground star.

[g]S/N ratio too low for accurate fitting; assuming the K-band value of $r_{\rm eff}$ suggests zero-point source contribution to the host galaxy itself, with the unresolved companion object accounting for ~20 per cent of the total flux.

[h]The presence of bright excess UV emission (both to the south-east of this galaxy and also to the north-west within it) prevents good fitting of the effective radius of this source in the *HST* filters. The K-band value is used to constrain the nuclear point source contribution in these filters.

mass is the sole cause of this difference between the samples, the more powerful radio sources would be expected to be hosted by ~75 per cent larger elliptical galaxies. Comparison of the results of RER98 (mean effective radius of 3.6 kpc for elliptical host galaxies, excluding the double source 6C 1129+37) with those of BLR98 for the 3CR galaxies (14.7 kpc) suggests a much larger difference than this, but the inclusion of the presence of nuclear point sources in our galaxy fitting procedure can greatly improve on this result.

The mean effective radius we derive for the $z \sim 1$ 6C galaxies is ~10.5 kpc, which is less than that of the 3CR data by a little under 50 per cent. This corresponds to an expected K-band magnitude difference of ~0.5 mag, in excellent agreement with the observed K–z relation.

However, although these results would indicate a difference in mean radii between the two samples, Kolmogorov–Smirnov (K–S) tests suggest that the distribution of radial sizes for the two

Table 2. Typical galaxy sizes for a number of different radio source samples. Columns 1–3 provide details of each sample: a reference, the radio source sample from which the data were selected and the mean redshift. Column 4 gives the median effective radius, and column 5 the mean effective radius and standard error on the mean. The average percentage nuclear point source contribution, where available, is listed in column 6. All data have been converted to the same cosmological model of $\Omega_0 = 0.3$, $\Omega_\Lambda = 0.7$ and $H_0 = 65 \text{ km s}^{-1} \text{ Mpc}^{-1}$ where necessary.

Reference	Sample	Redshift	Median r_{eff} (kpc)	Mean r_{eff} (kpc)	Point source percentage
This paper	6C	1.11	9.35	10.45 ± 1.94	16.1 ± 4.0 per cent
Pentericci et al. (2001)	MRC	2.06	5.85	5.96 ± 1.77	–
Zirm et al. (2003)	3C	1.16	8.19	8.85 ± 1.35	1.2 ± 0.5
BLR98	3C	0.93	15.1	14.72 ± 1.20	7.3 ± 2.7
McLure & Dunlop (2000)	3C	0.89	9.45	11.42 ± 1.55	–
McLure et al. (2004)	3C, 6C, 7C, TOOT	0.50	13.89	14.97 ± 0.98	–
McLure et al. (2004)	3C	0.49	17.88	19.41 ± 1.62	–
McLure et al. (2004)	6C	0.49	13.25	13.58 ± 1.53	–
McLure et al. (2004)	7C	0.53	11.15	11.21 ± 1.27	–
McLure et al. (2004)	TOOT	0.48	10.98	12.53 ± 1.67	–
Roche & Eales (2000)	3C (all sources)	0.20	9.56	15.72 ± 4.08	–
	3C (discs excluded)	0.20	10.56	17.34 ± 4.55	–
McLure et al. (1999)	RGs, RLQs, RQQs[a]	0.19	7.42	9.51 ± 1.03	–
McLure et al. (1999)	RGs only[a]	0.19	12.66	12.58 ± 2.27	–
Zirm et al. (2003)	3C	0.15	4.48	5.49 ± 1.11	–

Notes:[a]Full sample consists of a mixture of radio galaxies, radio loud quasars and radio quiet quasars.

samples are in fact not significantly different. In addition, alternative estimates of the mean radii for 3CR sources have suggested lower values than those of BLR98: McLure & Dunlop (2000) derived a mean radius of 11.4 kpc from WFPC2 observations of a subsample of the 3CR galaxies used by BLR98, and Zirm, Dickinson & Dey (2003) used NICMOS observations of 3CR galaxies to derive a mean radius of 8.85 kpc. These results, together with the lack of significance in the K–S test, suggest that the radii of the 3CR and 6C galaxies are very similar. The range of results obtained is not unsurprising given the small sizes of the samples which have been studied, and the observed large scatter within the two galaxy samples from which these data were drawn.

Our observed similarity in host galaxy properties is confirmed by other recent work on the wider radio galaxy population. A summary of the key results from a number of different studies of radio galaxy samples at different redshifts and radio powers has been collated in Table 2. Although not statistically significant, the average effective radii found for these data are typically somewhat larger than those of our 6C subsample. Continuing the comparison with lower redshift 3CR galaxies, matched in radio power to the $z \sim 1$ 6C subsample (e.g. McLure et al. 1999; Roche & Eales 2000), the emerging picture is that a radio source similar to our $z \sim 1$ 6C sample in power will be hosted by a ~ 10 kpc elliptical galaxy regardless of the cosmic epoch at which it exists. Although galaxy mass may play some role in explaining the drop in K-band luminosity between the 6C/3CR samples, it seems that it cannot account for it completely.

Despite this, there is still some evidence in favour of a mass–radio luminosity relationship. McLure et al. (2004) provide an analysis of four radio galaxy samples of different powers at $z \sim 0.5$. For these data, the 3CR sources were found to have larger sizes (median 17.9 kpc) than the 6C sources (13.3 kpc), which were in turn more massive than the still less powerful 7CRS (11.2 kpc) and TOOT (11.0 kpc) radio sources, suggesting a weak correlation between radio luminosity and bluge/black hole mass within their $z \sim 0.5$ sample. K–S tests on these data confirm that the 3CR sources are indeed larger on average than the 6C/7CRS/TOOT sources at a significance level of >95 per cent. There is no significant size
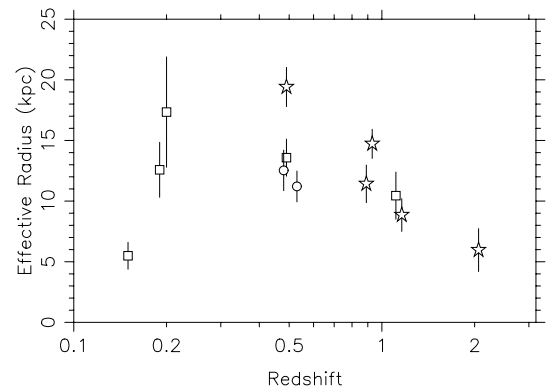
Figure 11. Mean effective radius versus redshift for the radio galaxy samples of Table 2. The symbols denote the typical radio luminosities of the samples: the circles have $L_{151} < 10^{26}$ W Hz^{-1} sr^{-1}, squares have $10^{26} < L_{151} < 10^{27}$ W Hz^{-1} sr^{-1}, and stars have $L_{151} > 10^{27}$ W Hz^{-1} sr^{-1}. Error bars are the standard error on the mean for each sample.

difference between the 3CR and 6C data alone, or between the 6C sources and the lower radio power 7CRS/TOOT sources, emphasizing the weakness of this trend and the ease with which it can be swamped by the relatively large scatter in galaxy properties within each sample. The 6C galaxies at $z \sim 0.5$ appear to be larger on average than those at $z \sim 1$, which if truly representative of evolution in the galaxy properties, could indicate continued growth (e.g. via mergers) of the host galaxy population at $z < 1$. However, the $z \sim 0.2$ sources appear comparable in size to those at $z \sim 1$, which suggests that the larger sizes of the $z \sim 0.5$ sources may simply be anomalous. We have also plotted the data presented in Table 2 as a function of redshift (Fig. 11). The scatter in the data is large, and we have not included any systematic errors arising from the different methods and quality of data sets used. However, this plot does provide a useful illustration of an apparent gradual growth of the host galaxy population, from $z \sim 2$ up to at least $z \sim 1$, perhaps continuing to later times.

A final interesting point of note is that given that any difference between the 6C and 3CR host galaxy masses is far less than their difference in radio power (a factor of $\sim$5 at $z \sim 1$), it might be expected that the contribution from a nuclear point source would on average be lower for the 6C sources; this assumes that any unresolved nuclear emission associated with the AGN scales with radio power. We find mean point source contributions of 16 ± 4 per cent and 7 ± 3 for the 6C and 3CR samples, respectively. Surprisingly, K–S tests show that the greater relative point source contribution for the 6C data is in fact weakly significant at the 90 per cent level, although owing to the small sample size this result could be dominated by one or two objects. Interestingly, if we compare the core–lobe ratio of radio flux between the 6C and 3CR subsamples (Best et al. 1997, 1999), the values obtained are very different. The 6C sources have an average core flux fraction of 0.026 (excluding the very high core fraction of the unusual radio source 6C 1217+36), whereas the mean 3CR galaxy core fraction is 0.0045. This could imply that the 6C sources are observed at an angle closer to the line of sight than the 3CR sources, and the AGN are less heavily obscured, thereby increasing the point source contributions to the observed 6C magnitudes.

The unresolved point source emission observed in many of the galaxies in our sample may be owing to several processes: the AGN itself, nuclear emission lines or an associated unresolved nuclear starburst. We have compared the nuclear point source contributions in the 6C and 3CR $z \sim 1$ samples with the emission line luminosities of our spectroscopic observations (Best, Röttgering & Longair 2000a,b; Inskip et al. 2002b,c), and find no correlation. This suggests that nuclear emission lines are unlikely to be responsible for the observed point source emission. Our data do not allow us to distinguish between the other two possibilities of AGN or nuclear starburst. The impact of this nuclear point source emission on the galaxy colours will be considered further in Paper III of this series.

3 THE ALIGNMENT EFFECT IN THE 6C SUBSAMPLE

3.1 Distributions of the excess UV emission

The aligned structures surrounding 6C and 3CR radio galaxies at $z \sim 1$ display a wide variety of different features. The most luminous features observed are bright knots of continuum emission; these are seen near several galaxies (e.g. 6C 1011+36, 6C 1129+37, 3C 356, 3C 368 and others). Another type of prominent feature often observed is a bright arc-like structure, extending from the host galaxy, and occasionally linked to other bright features. A particularly good example of such an arc can be seen in images of 3C280; arcs are also observed in the *HST* images of 6C 1017+37 and 1204+35. A third 6C radio source, 6C 1257+36, displays a small, very blue arc-like structure, apparently associated with a bright knot in the radio emission (Paper I). Fainter linear structures, or filaments of diffuse emission can be seen near, for example, 6C 0943+39 and 3C 352. Other commonly observed features are faint linear extensions or tails projecting out from the host galaxy, such as those observed in images of 6C 0825+34 and 3C 22. These are not, however, owing to optical emission from a radio jet. In general, some amount of faint diffuse emission is observed around the majority of sources. Usually, each source exhibits one or more of these distinct features. Whilst some sources appear completely passive (e.g. 6C 1100+35, 6C 1217+36 and 3C 65), after subtraction of the best-fitting host galaxy model we often see signs of excess emission towards or offset from the centre of the host galaxy in the residual image (e.g. 6C 1217+36 in particular).

In addition to the aligned emission observed around these sources, the appearance of several galaxies suggests that the UV emission from these sources has been affected by the presence of dust. Extensive dust lanes lying perpendicular to the radio axis, such as those observed in UV imaging observations of low-redshift radio galaxies (Allen et al. 2002; de Koff et al. 1996), could plausibly explain certain morphological features of the host galaxies of high-redshift radio sources such as 3C 252 and 3C 324 (Best et al. 1997; Longair, Best & Röttgering 1995), 6C 1204+35, and at still lower radio powers, 7C1748+6731 (Lacy et al. 1999). It is worth noting that although the presence of a dusk disc could create the false appearance of a small-scale alignment effect, this is only likely to be the case for a single object in our sample, 6C 1204+35.

The final feature revealed by the imaging observations is the presence of other nearby galaxies which may lie at the same redshift. Four of the 11 6C sources have companion galaxies at a close projected distance ($<$20 kpc; see Paper I in this series); a few of these sources clearly seem likely to be interacting with their companions. Similarly, a number of the $z \sim 1$ 3CR sources appear to have nearby companions (Best 1996); in several cases companion galaxies show evidence (e.g. increased star formation) for having been perturbed by the growing radio source. This issue will be discussed in more depth in Paper III of this series.

Whilst the infrared emission of the $z \sim 1$ 3CR host galaxies has been found to show a weak alignment effect (Zirm et al. 2003; BLR98 and references therein), we do not see any noticeable alignment in the *K*-band for our 6C subsample (nor is one seen in the case of low-redshift 3CR sources (de Koff et al. 1996; Martel et al. 1999), for which the alignment effect is weaker than at high redshifts at all wavelengths). The percentage contribution of the IR aligned component at high redshifts is known to be relatively low in any case: BLR98 and Rigler et al. (1992) find typical contributions of 11 and 10 per cent of the total IR flux, respectively. Although this in itself is insufficient to account for the *K*-band magnitude difference between the $z \sim 1$ 6C and 3CR samples, the infrared aligned component is still notable by its absence in the 6C subsample.

Having modelled the galaxy morphologies, the simplest method of quantifying the aligned emission is to evaluate the residual flux within some aperture. For the sources for which we have adequate galaxy models in the rest-frame UV, the resulting residual flux owing to excess UV emission within a 4-arcsec diameter aperture has been determined, and is tabulated in Table 3.

3.2 Quantifying the alignment effect

A very basic analysis of galaxy colours in different filters can be useful for quantifying the total excess UV emission, but it is also of crucial importance that the spatial distributions of the extended emission regions are understood. In particular, the total size of the extended structures and the degree to which they are aligned with the radio source axis vary greatly within both the 6C and 3CR subsamples. The strength of the alignment effect can be quantified using measurements of these different features, using the method of BLR98. This utilizes the difference in position angles of the radio axis and the aligned emission, and the total elongation of the extended structures.

The *alignment strength* is defined as

$$a_s = \epsilon \left(1 - \frac{\Delta\theta}{45} \right). \tag{1}$$

Here ϵ is the ellipticity of the rest-frame UV emission on the *HST* images; this is defined as $\epsilon = [1 - q^2/p^2]^{1/2}$, where p and q are

Table 3. Flux in residual images after subtraction of model galaxies. Results are given as a percentage of the total 4 arcsec diameter flux (column 3) and as a magnitude correction between the total flux in the aperture and the flux from the model galaxy alone (column 4). The data for 6C 1129+37 are presented in italics, as the accuracy of the host galaxy subtraction is unclear for this source.

Source	Filter	Residual flux (per cent)	Magnitude correction
6C 0825+34	*F814W*	–	–
6C 0943+39	F702W	39 ± 4	0.55 ± 0.04
6C 1011+17	F702W	20 ± 3	0.24 ± 0.03
6C 1017+37	F702W	22 ± 2	0.26 ± 0.02
6C 1019+39	F814W	6 ± 1	0.07 ± 0.01
	F606W	4 ± 2	0.05 ± 0.02
6C 1100+35	F814W	4 ± 2	0.04 ± 0.02
6C 1129+37	*F702W*	*63 ± 4*	*1.09 ± 0.05*
6C 1204+35	F814W	28 ± 3	0.36 ± 0.03
6C 1217+36	F814W	10 ± 3	0.11 ± 0.02
	F606W	9 ± 2	0.10 ± 0.03
6C 1256+36	F702W	43 ± 6	0.62 ± 0.06
6C 1257+36	F814W	5 ± 2	0.05 ± 0.02
	F606W	36 ± 4	0.49 ± 0.04

Table 4. Table of alignment strengths and component alignment strengths for the 6C subsample. The first two columns list the sources, and the filters used for the observations. Column 3 gives the measured number of bright components in the data; where the radio source has a close companion, we also list (in parentheses) the value of N_c after removal of the companion object. The ellipticity and position angle of the fitted ellipses are given in columns 4 and 5, respectively. Column 6 lists the difference in position angles between the radio axis and the aligned emission. These parameters are then used to determine the alignment strength (a_s, column 7) and the component alignment strength (a_c, column 8) for each observation.

| Source	Filter	N_c	ϵ	θ	ΔPA	a_s	a_c
6C 0825+34	F814W	1	0.47	−72°	26°	0 198	0 198
6C 0943+39	F702W	1	0.69	−34°	17°	0 429	0 429
6C 1011+36	F702W	2	0.40	−44°	28°	0 151	0 302
6C 1017+37	F702W	1	0.32	70°	1°	0 313	0 313
6C 1019+39	F606W	2	0.22	−87°	42°	0 015	0 030
	F814W	1	0.29	−76°	53°	−0 052	−0 052
6C 1100+35	F814W	1	0.10	15°	82°	−0 082	−0 082
6C 1129+37	F702W	6(6)[a]	0.47	56°	18°	0 282	1 692
6C 1204+35	F814W	1	0.57	2°	17°	0 355	0 355
6C 1217+36	F606W	1	0.12	50°	9°	0 096	0 096
	F814W	1	0.20	30°	11°	0 151	0 151
6C 1256+36	F702W	2(1)[b]	0.40	55°	15°	0 267	0 533
6C 1257+36	F606W	2	0.38	−32°	16°	0 245	0 490
	F814W	1	0.39	−40°	25°	0 173	0 173

Notes. [a]The companion galaxy to this source forms only part of one of the six discrete components, and its removal would not affect the value of N_c for this source.
[b]For 6C 1256+36, the removal of the companion object would reduce N_c from 2 to 1.

the lengths of the semimajor and semiminor axes respectively of the ellipse which provides the best fit to the large-scale UV excess. $\Delta\theta$ is the difference in the position angles of the radio axis and the semimajor axis of the rest-frame UV emission. The alignment strength can therefore have values in the range $-1 \leqslant a_s \leqslant 1$. Sources with $\Delta\theta < 45°$ have a positive value for a_s. Sources which are misaligned with the radio axis have $\Delta\theta > 45°$ and $-1 \leqslant a_s \leqslant 0$. For perfectly round galaxies, $\epsilon = 0$ and $a_s = 0$.

In order to determine the orientation and ellipticity of the emission, ellipses were fitted to the *HST* images using the IRAF package ELLIPSE. The *HST* images were first smoothed, using a Gaussian with $\sigma = 0.2$ arcsec. By smoothing the data, consistent fits to the relative elongation and alignment of the irregular structures observed around these sources could be obtained over a large range of different size ellipses. The aim of this was to obtain a consistent fit to the galaxy, whilst including as much of the aligned emission as possible without introducing too much noise from the sky background. Without first smoothing the data, consistent fits would be unobtainable, as the presence of a bright peak would skew the results at a given fitting radius. This Gaussian width was carefully chosen to allow accurate fitting of the data without over smoothing. The orientation and ellipticity of the galaxies were taken from the average parameters of several successive fitted ellipses, with the requirement that these did not vary significantly, and included the majority of the flux from the galaxy and any aligned emission. Once the fitting was completed, the orientation of the emission was compared with the radio axis, and a measure of $\Delta\theta$ obtained.

This process is relatively straightforward and it gave clear, consistent results for the majority of sources. In the case of 6C 1204+35, there is some doubt as to whether the bright region of emission roughly 4 arcsec to the north of the host galaxy is aligned emission, or a companion galaxy. Ellipses were fitted to the emission from the host galaxy without attempting to include this feature. The full results of our analysis of the 6C subsample aligned structures are presented in Table 4.

The alignment strengths of the 6C galaxies are very similar to those of 3CR sources at the same redshifts and radio sizes. This can be seen in Fig. 12, which plots alignment strength versus redshift

and radio size, for observations made in the filter closest to a rest-frame wavelength of 3500 Å. Where observations were made in two filters which straddle a rest-frame wavelength of 3500 Å, a weighted interpolation has been used in order to derive the value at 3500 Å. Both samples seem to show a peak in the alignment strength at a redshift of just over $z = 1$. This correlates well with the minimum value in F707W−K (see Paper III), observed at $z \sim 1.1$; the galaxies displaying the strongest alignment effect are also bluer in colour owing to this excess UV emission. The excess UV flux determined in Section 3.1 is also found to be strongly correlated with the alignment strength, at a significance level of >99 per cent (excluding 6C 1129+37, as the host galaxy cannot be easily modelled in the rest-frame UV).

In addition to the observed variations with luminosity and redshift, the alignment strength is also at a maximum for the smaller radio sources. Including all 6C and 3CR sources, alignment strength is anti-correlated with radio size in a Spearman rank correlation test at a significance level of >96 per cent. This is as expected, given the greater extent of the aligned structures observed around these smaller radio sources (Best et al. 1996; Paper I; this paper). The calculated alignment strengths are based on measurements of the difference in position angles between the radio and UV emission, and the ellipticity of the smoothed images. For the galaxies in both samples in the redshift range $0.85 < z < 1.5$, the measured ellipticities are similar at $\epsilon \sim 0.35$. This suggests that the extended structures are also equally well aligned in both samples.

Whilst the extended features observed around distant radio sources in both samples are similar, one major difference is observed. Extended strings of bright, knotty emission, well aligned with the radio axis (such as those observed in 3C 266, 3C 324 and 3C 368) are less frequently seen in the observations of the 6C
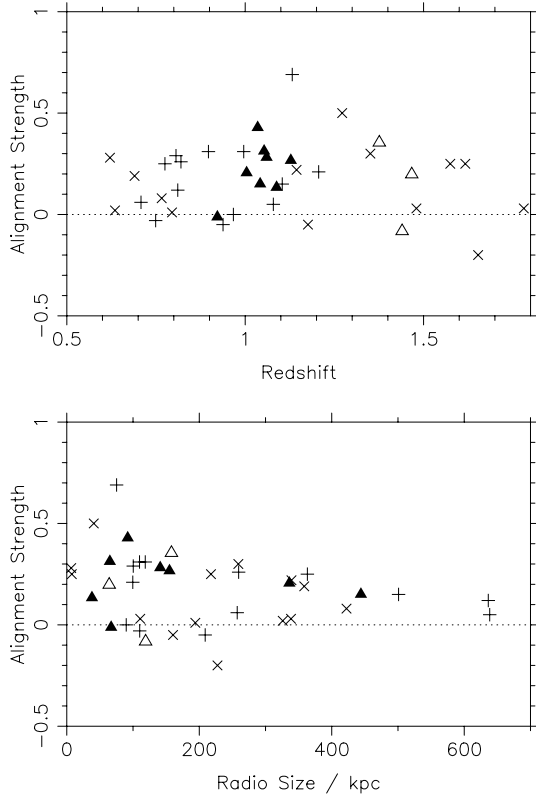
Figure 12. Alignment strength versus redshift (top) and radio size (bottom) for the 6C and 3CR radio galaxies at $z \sim 1$. 6C sources are represented by the triangles: filled triangles represent the eight sources in the $0.85 < z < 1.2$ spectroscopic sample (Inskip et al. 2002b). 3CR sources are represented by crosses: the sources in the $0.7 < z < 1.25$ 3CR spectroscopic sample (Best et al. 2000a) are marked by '+', with the remaining galaxies marked by '×'.

subsample. A visual inspection of the *HST* images suggests that where these features are observed around the 6C galaxies, they include fewer discrete components and are generally located closer to the host galaxy; even 6C 1129+37 displays less extreme features than those of many 3CR galaxies at the same redshift.

We have therefore quantified some of the morphological differences between the two subsamples. Owing to the strong variations observed with redshift in the 3CR subsample, this analysis has been restricted to the 13 galaxies in the redshift range of the 6C subsample, $0.85 < z < 1.5$. First, we consider the number of bright components in the images of the 6C and 3CR galaxies, and also the mean separation of these luminous features.

The number of discrete components of emission was determined using the same definition as Best (1996), but with some added restrictions required by the fainter 6C galaxies. The minimum flux level for a bright component has been set at 10 per cent of the maximum flux, or at 3σ above the sky noise level, whichever is larger. This prevents sky noise being identified as a spurious bright component. The IRAF package IMREPLACE was used to blank out pixels below this cut-off flux level, thus identifying the potential bright components. Any potential bright component was then examined using a lower cut-off flux level of 5 per cent of the maximum emission. Confirmation was only given to components which covered at least four adjacent pixels and were unconnected to any other bright component at this lower flux level.

Table 5. Distribution of aligned emission features. The first half of this table tabulates the distribution of the number of bright emission components for the 6C and 3CR galaxies in the redshift range $0.85 < z < 1.5$. Different values of N_c were obtained in different filters for two sources; in this analysis we classify 6C 1019+39 as having $N_c = 2$, and 6C 1257+36 as $N_c = 1$. We do not know whether the unresolved feature adjacent to 6C 1256+36 lies at the same redshift or is a foreground object, and have classed this object as $N_c = 2$ rather than 1. The second half compares the mean component separation for $N_c = 2$ and $N_c \geqslant 3$. The final section quantifies the range of physical extents for the aligned emission across the samples, assigning each galaxies to one of four different size ranges. The emission around the 3CR sources is typically more extensive, as expected given their larger average value of N_C.

	6C sample	3CR sample
Number of bright components		
$N_c = 1$	7	2
$N_c = 2$	3	2
$N_c \geqslant 3$	1	9
Mean comp. separation		
$N_c = 2$	8 kpc	6 kpc
$N_c \geqslant 3$	15 kpc	18 kpc
Physical extent		
$D \leqslant 10$ kpc	4	3
10 kpc $< D \leqslant 20$ kpc	4	1
20 kpc $< D \leqslant 30$ kpc	0	4
30 kpc $< D$	3	5

Our results (see also Table 5) can be summarized as follows.

(i) Seven 6C sources have a single bright component, three have two bright components,[2] but only one source displays more than one additional bright feature.

(ii) Conversely, only two of the 13 3CR sources have a single bright component, and two have a second bright component. The remaining nine 3CR sources display three or more bright features.

(iii) The mean separation of bright components for galaxies with $N_c = 2$ is less than 10 kpc on average in both samples.

(iv) If more than one additional bright feature is observed, the average distance of the bright components from the galaxy is nearly twice as high, at ≈ 15 kpc for the 6C sample, and ≈ 18 kpc for the 3CR sample.

Another useful parameter developed in Best (1996) is the *component alignment strength*, a_c. This parameter not only provides a measure of the degree of alignment, but also the flux in the aligned features, and particularly the importance of bright knots in the aligned emission. The component alignment strength is given by

$$a_c = N_c a_s = N_c \epsilon \left(1 - \frac{\Delta\theta}{45} \right), \qquad (2)$$

where N_c is the number of bright emission components.

The component alignment strengths for the 6C and 3CR galaxies are plotted as a function of redshift and radio power in Fig. 13. Once again, similar trends are observed for both the 6C and the 3CR galaxies, with a peak in the component alignment strength at $z \sim 1.1$. The slight decrease beyond this redshift is owing to the decreasing sensitivity of the higher redshift observations. Any anti-correlation with radio size is weaker, and is statistically insignificant. We again

[2] If the unresolved feature adjacent to the host galaxy of 6C 1256+36 is a foreground star, this gives eight objects with $N_c = 1$, and only two with $N_c = 2$.
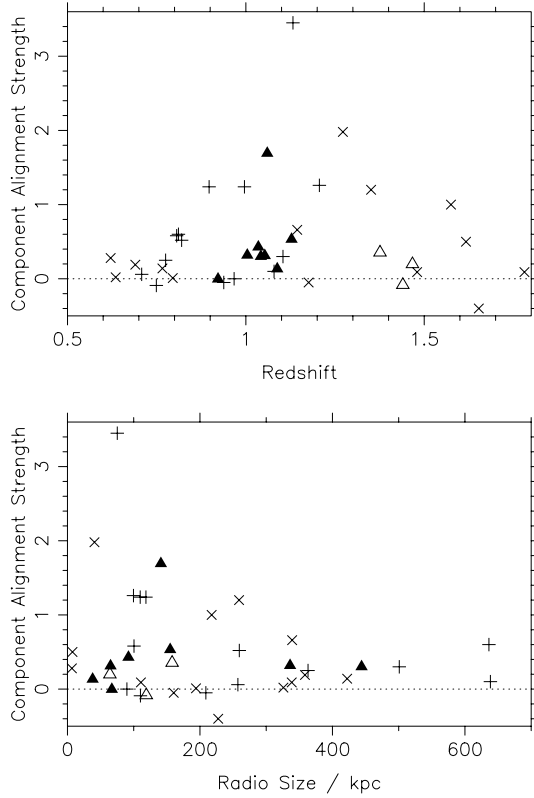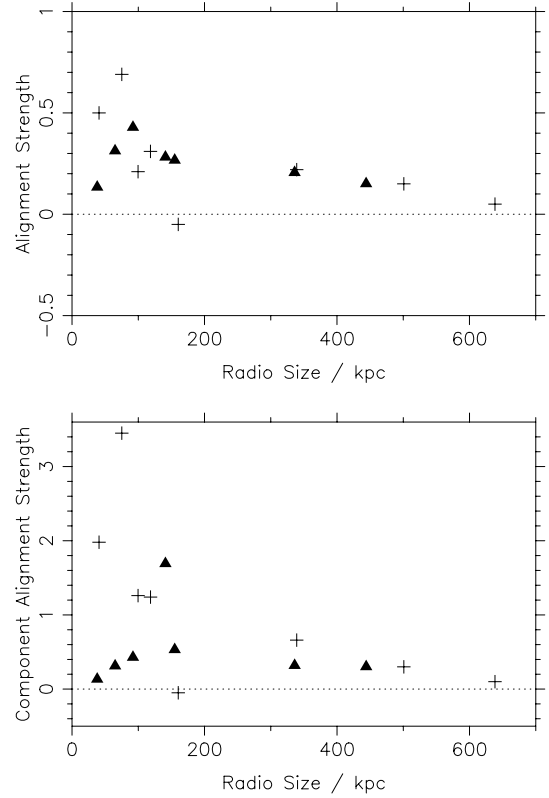
Figure 13. Component alignment strength versus redshift (top) and radio size (bottom) for the 6C and 3CR radio galaxies at $z \sim 1$. Symbols are as in Fig. 12.
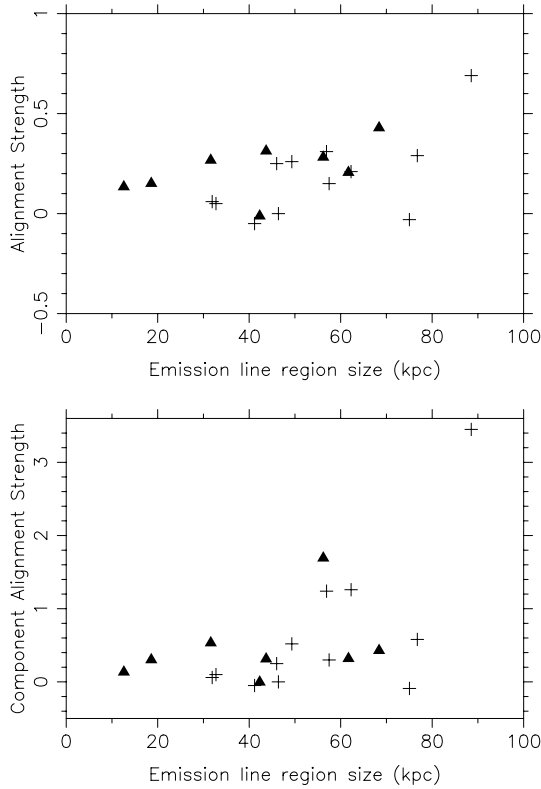

Figure 14. (top) Alignment strength versus radio size and (bottom) component alignment strength versus radio size (for sources with $1.0 < z < 1.3$ only). 6C sources are represented by the triangles, and 3CR sources by the crosses.

see a strong (>99.5 per cent significant) correlation between component alignment strength and the excess UV flux in our residual images (again excluding 6C 1129+37). The component alignment strengths of the 6C sources are generally much lower than those of the 3CR sources, and where a value of $N_C > 1$ is observed in the 6C sample, this is not so clearly biased towards smaller radio sources as is seen for the 3CR sources. Multiple bright knots of emission are rarer in the 6C data (Table 5): at $z \sim 1$ the average number of bright components is 1.7 for the 6C sample, and 2.7 for the 3CR sample.

Although 6C and 3CR sources at the same redshift have similar values for the measured strength of the alignment effect, the measured component alignment strengths were generally less for the 6C sample. The extended structures of the 3CR sources are clearly more 'knotty' on average than 6C sources of a similar radio size. It is also interesting that where large number of discrete components are seen, their spatial distributions are similar in both samples, regardless of radio power.

3.3 The alignment effect at $z \sim 1$

The differences between the 6C and 3CR samples become clearer when we consider a restricted redshift range. Fig. 14 displays the variation in alignment strength and component alignment strength with radio size, for the sources in the redshift range $1.0 < z < 1.3$. At these redshifts, the alignment effect has generally reached its maximum observed strength, but the data do not yet suffer from high-redshift sensitivity problems. The alignment strengths for the 3CR data are anti-correlated with radio size at a significance level of >95 per cent; adding the 6C data increases this to >97.5 per cent.

Whilst both the 6C and the 3CR sources show a very similar result for the variation in a_s with radio size, the results for a_c clearly show that the smaller 6C sources lack the knotty structures observed in the 3CR sample. The 3CR sources show a 99 per cent significant anti-correlation between a_c and radio size; the strength of this correlation is reduced to ~95 per cent with the inclusion of the 6C data points.

If the emission which produces the bright knots of emission is owing to line or nebular continuum emission, the more powerful 3CR sources should indeed display these features more frequently. However, an analysis of the data for two of the sources in the 6C subsample shows that whilst the diffuse extended emission surrounding 6C 0943+39 is dominated by line emission, only a small fraction of the bright knotty emission surrounding 6C 1129+37 can be attributed to such processes. This result implies that other mechanisms are responsible for the bright knotty emission predominantly observed around the smaller radio sources. The evolution with radio source size of the 3CR aligned emission has previously been interpreted as being consistent with the effects of the aging of a young stellar population, whose formation was triggered by the passage of the expanding radio source (Best et al. 1996). Should this indeed be the case, the morphological differences between the aligned emission in the 6C and 3CR subsamples suggests that the drop in radio power has implications for the efficiency and/or outcome of these processes.

It is particularly useful to contrast our imaging with the results of our spectroscopic observations of the 6C and 3CR $z \sim 1$ subsamples (Best et al. 2000a,b; Inskip et al. 2002b,c). To summarize, the spectra of these sources show that the ionization state and kinematic

Figure 15. (top) Alignment strength versus EELR size and (bottom) component alignment strength versus EELR size (for sources in the spectroscopic samples of Inskip et al. (2002b) and Best et al. (2000a,b)). 6C sources are represented by the triangles, and 3CR sources by the crosses.

properties of the gas in the extended emission-line regions (EELRs) vary independently with both radio power and size. The EELRs of smaller radio sources are more luminous and extensive, and are best explained by a contribution from shock ionization associated with the expanding radio source as well as from AGN photoionization. Partial rank analysis of 6C and 3C spectra (Inskip et al. 2002c) showed that the gas kinematics are also more extreme for the sources at higher redshifts, independently of the effects of radio source power and size/age. These results suggest that there is some evolution of the local intergalactic medium (IGM), and that either the distribution and density of gas clouds varies with redshift, or that interactions/shocks between the IGM and the radio source are less important at later cosmic epochs. Whilst the alignment effect is often observed around lower redshift sources, it is generally less extreme than that surrounding high-z sources of similar radio power (Allen et al. 2002; Dey & van Breugel 1993), indicating clear evolution in the mechanisms which produce the alignment effect as well as the expected dependence on radio power.

The properties of the EELRs seem to be closely linked to the alignment effect. The small radio sources in both samples which do not show a strong UV alignment effect are usually those which have passive, quiescent emission-line regions. However, where shocks are seen to boost the emission-line luminosity, kinematics and overall extent of the emission region, we also find that these sources often display a strong alignment effect. Although the extended line emission does not account for a large proportion of the total flux observed in the rest-frame UV (typically a few per cent up to a maximum of 20 per cent in some sources), the sources which display the most extreme alignment effect also have the largest emission-line

Table 6. Significance levels of correlations between EELR size and either alignment strength (a_s) or component alignment strength (a_c). The results are presented for calculations using both the observed (top) and the corrected (bottom) 6C EELR sizes.

Correlation using observed 6C EELR sizes	a_s (per cent)	a_c (per cent)
Full data	>90	>95
Data with $1.0 < z < 1.3$	>95	>95
Correlation using corrected 6C EELR sizes	a_s	a_c
Full data	>95	>99.5
Data with $1.0 < z < 1.3$	>99	>99

regions: a feature which is itself closely linked to the importance of shocks (Fig. 15). Both a_s and a_c are correlated with emission-line region size (details in Table 6). These correlations are strengthened if we either restrict the data to the matched set of objects lying between $1.0 < z < 1.3$, or if we scale the 6C emission-line region sizes upwards by 25 per cent to reflect the lower sensitivity of the spectroscopic observations (Inskip et al. 2002b). There is a clear change between the sources which show a strong alignment effect when small and young, to the more passive evolved sources that they will become at later times. This trend for alignment strength and component alignment strength in particular to be correlated with emission-line region size is actually stronger than that with radio size. Despite the fact that the trends with radio size for the alignment effect are weaker for the 6C sample, this is a good indication that the underlying trends observed for the 3CR galaxies still hold true at lower radio powers, and that the presence of shocks in the extended emission regions may be a driving factor in producing the most extreme alignment effects.

4 DISCUSSION

The analysis of the morphologies and alignment strengths of $z \sim 1$ 6C and 3CR radio galaxies has led to a number of interesting results.

(i) The 6C host galaxies at $z \sim 1$ are best described as de Vaucouleurs ellipticals. Fitting with Sérsic profiles gives a mean value of $n \sim 4$ for the sample; the range of values determined for n ($2 \lesssim n \lesssim 6$) is comparable to that found by Zirm et al. (2003) in their similar analysis of 3CR sources at $z \sim 1$. It is noteworthy that the two sources which have $n > 4$ are amongst the three most luminous in the sample; larger values of n are frequently observed to be correlated with the mass/luminosity of the host galaxy (e.g. Graham & Guzmán 2003).

(ii) Typically, the 6C sources have effective radii of $\sim$9–10 kpc and an average unresolved nuclear point source contribution of 16 per cent in the K band. The values of these parameters are comparable to those of low-redshift radio galaxies matched in radio power, and also to more powerful radio sources at the same redshift.

(iii) The measured alignment strengths, and the variations in this parameter with both redshift and radio size are almost identical for both the 6C and the 3CR $z \sim 1$ subsamples. Both a_s and a_c peak at a redshift of $z \approx 1.1$, and are anti-correlated with radio source size. Similar ellipticities are measured for the smoothed images, and the extended structures are equally well aligned with the radio axis.

(iv) On average, the component alignment strength is lower for the 6C sources. These display fewer bright components, and their aligned structures are generally less extensive.

(v) However, for sources matched in radio power, the higher redshift sources display a stronger alignment effect. This reflects the

decreasing importance of interactions at low redshifts, and also the possible evolution of the distribution of material in the surrounding IGM.

(vi) The observed trend for the smaller 3CR sources to display brighter, more extensive and better aligned morphologies (Best et al. 1996) is clearly not as strong for the galaxies in the 6C subsample, which generally have less extreme morphologies.

(vii) Regardless of radio size, the sources which display an extreme alignment effect also have the most extensive emission regions; these are the sources for which shocks are most important.

Our results add further weight to the picture that the various features of the alignment effect depend strongly on both redshift and radio source power. Radio power remains an important factor at lower redshifts, as is evident from the study of a sample of still less powerful 7C radio galaxies at $z \sim 0.7$ (Lacy et al. 1999). For the 7C systems, aligned emission is still observed, but is substantially weaker than that of the matched sample of more powerful 3CR sources at the same redshift. The percentage aligned flux is found to be lower (7 per cent for 7C cf. 18 per cent for 3C, at wavelengths slightly longer than the 4000 Å break), and the excess emission exists on smaller spatial scales than for the higher radio luminosity 3CR sources at the same redshift. Additionally, neither sample displays any trends between alignment effect and radio source size; the luminous clumpy features most likely to be responsible for the radio size trends observed in the 3CR $z \sim 1$ subsample are far less common at lower redshifts and/or radio powers. In terms of evolution with redshift, the 6C alignment effect at $z \sim 1$ is more frequent and noticeably stronger than that observed for galaxies of a similar radio luminosity at lower redshift. Dey & van Breugel (1993) observed significant UV alignment effects in only 30 per cent of low-redshift systems; similar results are seen in other low-redshift studies (e.g. de Koff et al. 1996).

Given that the alignment effect clearly varies in strength with radio source power as well as redshift, one might expect its behaviour to be predictable. Of the various mechanisms proposed to explain the alignment effect, several should scale with radio power. [O II] emission and the bulk kinetic power of the radio jet are both observed to scale with radio source luminosity to the power of $\sim 6/7$, over a wide range of source powers and redshifts (Rawlings & Saunders 1991; Willott et al. 1999). Scattered AGN emission and total line emission are therefore also expected to increase with the power of the radio source. On the other hand, star formation induced by the passage of the radio source jets may be favoured in the case of lower power radio sources (perhaps explaining the strong alignment effects observed in the case of the high-redshift 6C sources), where the bulk kinetic energy carried by the jets is correspondingly lower (Lacy et al. 1999). However, this does not rule out star formation induced by lower velocity bulk motions associated with backflows or the sideways expansion of the radio cocoon in the case of more powerful sources. Given the strong alignment effects observed for both $z \sim 1$ subsamples, the optical/UV alignment effect clearly depends on a number of other factors in addition to radio power, which themselves become unable to induce such a strong alignment effect at lower redshifts.

The emission at longer wavelengths is also worthy of further discussion. The lack of any IR alignment effect in our 6C subsample suggests that the long wavelength tail of the alignment effect does indeed scale most strongly with radio power. However, the long-wavelength alignment effect cannot account for differences in K-band emission between the 6C and 3CR samples, nor is it sufficient to explain the fact that the host galaxies of high-redshift radio sources are more luminous than expected based on the predictions of passive evolution models (Inskip et al. 2002a). The strength of any nuclear point source contribution cannot be responsible, as the point source percentage in the K band is similar for both $z \sim 1$ samples, regardless of radio power. Variations in K-band luminosity cannot easily be explained by host galaxy mass either; the 6C host galaxies are massive ellipticals very similar in size to those of other radio galaxy samples matched in either radio power or redshift. Below $z \sim 2$, the radio source host galaxy population appears remarkably uniform, with scale sizes in the region of 10 kpc: well below those of brightest cluster galaxies, but still larger than is typical for normal low-redshift ellipticals. This is in good agreement with the apparent passive evolution of the lower power radio sources in the K-band magnitude–redshift (discussed in detail in Inskip et al. 2002a).

The only remaining possibility is a significant proportion of young stars in the host galaxies of the more powerful sources. The problem with this approach is that the presence of a young stellar population of $\lesssim 10^8$ yr in age is itself constrained by the shorter wavelength galaxy colours to a fairly limited proportion of the host galaxy total stellar mass (<5 per cent, equivalent to a maximum 0.5-mag increase in K-band luminosity; BLR98 and Inskip et al. 2002a). However, recent research (e.g Tadhunter et al. 2002; Wills et al. 2002; Tadhunter et al. 2005) has identified the clear presence of older (0.1–2 Gyr), often reddened, young stellar populations, which could provide an increase in the observed IR emission without overly boosting the rest-frame UV beyond the observational limits. Such a scenario would also fit in well with the recent results from the Sloan Digital Sky Survey, which found that the highest luminosity AGN were hosted by galaxies with relatively young stellar populations (Kauffmann et al. 2003).

We have investigated the influence of unreddened young stellar populations on the galaxy emission. Using the GISSEL spectral synthesis models of Bruzual & Charlot (2003), we find that in order to produce a 0.5-mag increase in K-band magnitude whilst avoiding large increases in the rest-frame UV emission from the host galaxy, the young stellar population is required to contain ~ 20 per cent of the host galaxy mass and be over 0.5 Gyr in age, i.e. significantly older than the radio source. Such an age could argue against any direct link with radio source power, and it is not obvious that this could explain any K-band magnitude difference between the 6C and 3CR data. However, if such a starburst was associated with a merger event which led to the subsequent triggering of the radio source/AGN activity, then the exact details of that merger could provide a link between any young stellar population and the power of the resulting radio source. It is also possible that the more diffuse aligned emission (which displays less radio power dependence) could be associated with such older, merger-related starbursts. West (1994) suggests that mergers occur anisotropically and that the radio source jets are likely to be orientated in alignment with the surrounding matter distribution, thereby leading to an alignment with a young stellar population which could be older than the radio source itself. On top of this, other processes (including later radio source/jet-induced star formation) would be responsible for producing the more luminous, clumpy aligned emission, which does show a strong dependence on both radio source power and age. In addition to a strong UV excess, such very recent star formation ($10^7 - 5 \times 10^7$ yr in age) could also generate an increase in flux at longer wavelengths sufficient to explain the fact that these galaxies are typically 0.5-mag brighter than the predictions for purely passively evolving systems at $z \sim 1$ (Inskip et al. 2002a). However, for consistency with our observed data, for most sources such a young starburst would be limited to a few per cent of the total galaxy mass, and would need to be reddened by

an $E(B - V)$ of typically 0.2–0.6. These issues will be considered in greater depth in Paper III of this series.

We expect that the most likely solution for explaining the evolution of the K-band galaxy properties is a combination of several factors: smaller variations in galaxy mass, recent star formation and contamination by processes associated with the radio source activity/alignment effect. At higher redshifts, it is likely that increased merger activity goes hand in hand with the presence of powerful radio galaxies and ongoing star formation (e.g. studies of ultraluminous infrared galaxies: Genzel et al. 2001; Tacconi et al. 2002; Bushouse et al. 2002). The morphologies of high-redshift ($z > 3$) radio sources are clearly disturbed, multicomponent systems, whilst at slightly lower redshifts ($z \sim 2$) although the galaxies give the appearance of settled elliptical systems, their typical scale sizes ($\sim$6 kpc) are very much smaller than those of radio sources at $z \sim 1$ (van Breugel et al. 1998; Pentericci et al. 1999), suggesting that they have not yet completed their process of assembly. It is certainly plausible that such processes are still affecting the lower redshift $z \lesssim 1$ systems on a smaller scale, but more so in the case of the most luminous radio sources such as the $z \sim 1$ 3CR galaxies, which also display the most extreme examples of the alignment effect.

ACKNOWLEDGMENTS

REFERENCES

Allen M. G. et al., 2002, ApJS, 139, 411

Best P. N., 1996, in Bremer M., Carilli C., Röttgering H., van der Werf P., eds, Astrophys. Space Sci. Library Vol. 206, Cold Gas at High Redshifts. Kluwer Academic Publishers, Dordrecht, p. 403

Best P. N., Longair M. S., Röttgering H. J. A., 1996, MNRAS, 280, L9

Best P. N., Longair M. S., Röttgering H. J. A., 1997, MNRAS, 292, 758

Best P. N., Longair M. S., Röttgering H. J. A., 1998, MNRAS, 295, 549

Best P. N., Röttgering H. J. A., Longair M. S., 2000a, MNRAS, 311, 1

Best P. N., Röttgering H. J. A., Longair M. S., 2000b, MNRAS, 311, 23

Bruzual G., Charlot S., 2003, MNRAS, 344, 1000

Bushouse H. et al., 2002, ApJS, 138, 1

Chambers K. C., Miley G. K., van Breugel W. J. M., 1987, Nat, 329, 604

Cimatti A., di Serego Alighieri S., Fosbury R. A. E., Salvati M., Taylor D., 1993, MNRAS, 264, 421

de Koff S., Baum S. A., Sparks W. B., Biretta J., Golombek D., Macchetto F., McCarthy P., Miley G. K., 1996, ApJS, 107, 621

Dey A., van Breugel W., 1993, BAAS, 182.0421

Dickson R., Tadhunter C., Shaw M., Clark N., Morganti R., 1995, MNRAS, 273, L29

Dunlop J. S., 1999, in Röttgering H., Best P. N., Lehnert M. D., eds, The Most Distant Radio Galaxies. Royal Netherlands Academy of Arts and Sciences, Amsterdam, p. 71

Eales S. A., Rawlings S., 1996, ApJ, 460, 68

Genzel R., Tacconi L. J., Rigopoulou D., Lutz D., Tecza M., 2001, ApJ, 563, 527

Govoni F., Falomo R., Fasano G., Scarpa R., 2000, A&A, 353, 507

Graham A. W., Guzmán R., 2003, AJ, 125, 2936

Inskip K. J., Best P. N., Longair M. S., MacKay D. J. C., 2002a, MNRAS, 329, 277

Inskip K. J., Best P. N., Rawlings S., Longair M. S., Cotter G., Röttgering H. J. A., 2002b, MNRAS, 337, 1381

Inskip K. J., Best P. N., Röttgering H. J. A., Rawlings S., Cotter G., Longair M. S., 2002c, MNRAS, 337, 1407

Inskip K. J., Best P. N., Longair M. S., Rawlings S., Röttgering H. J. A., Eales S. A., 2003, MNRAS, 345, 1365 (Paper I)

Kauffmann G. et al., 2003, MNRAS, 346, 1055

Kormendy J., Richstone D., 1995, ARA&A, 33, 581

Lacy M., Ridgway S. E., Wold M., Lilje P. B., Rawlings S., 1999, MNRAS, 307, 420

Longair M. S., Best P. N., Röttgering H. J. A., 1995, MNRAS, 275, L47

McCarthy P. J., van Breugel W. J. M., Spinrad H., Djorgovski S., 1987, ApJ, 321, L29

McCarthy P. J., Spinrad H., van Breugel W. J. M., 1995, ApJS, 99, 27

McLure R. J., Dunlop J. S., 2000, MNRAS, 317, 249

McLure R. J., Kukula M. J., Dunlop J. S., Baum S. A., O'Dea C. P., Hughes D. H., 1999, MNRAS, 308, 377

McLure R. J., Willott C. J., Jarvis M. J., Rawlings S., Hill G. J., Mitchell E., Dunlop J. S., Wold M., 2004, MNRAS, 351, 347

Mahabal A., Kembhavi A., McCarthy P. J., 1999, ApJ, 516, L61

Martel A. R. et al., 1999, ApJS, 122, 81

More J. J., 1977, in Watson G. A., ed., Lecture Notes in Mathematics 630, Numerical Analysis. Springer-Verlag, Berlin

More J. J., Wright S. J., 1993, Frontiers in Applied Mathematics 14. Soc. Industrial & Appl. Math, Philadelphia

Pentericci L., Röttgering H. J. A., Miley G. K., McCarthy P. J., Spinrad H., van Breugel W. J. M., Macchetto F., 1999, A&A, 341, 329

Pentericci L., McCarthy P. J., Röttgering H. J. A., Miley G. K., van Breugel W. J. M., Fosbury R., 2001, ApSS, 135, 63

Rawlings S., Saunders R., 1991, Nat, 349, 148

Rigler M. A., Lilly S. J., Stockton A., Hammer F., Le Fèvre O., 1992, ApJ, 385, 61

Roche N., Eales S. A., 2000, MNRAS, 317, 120

Roche N., Eales S. A., Rawlings S., 1998, MNRAS, 297, 405

Sérsic J. L., 1968, Atlas de Galaxias Australes. Observatorio Astronomico, Córdoba

Smith E. P., Heckman T. M., 1989, ApJ, 341, 658

Spinrad H., Dey A., Stern D., Dunlop J., Peacock J., Jimenez R., Windhorst R., 1997, ApJ, 484, 581

Tacconi L. J., Genzel R., Lutz D., Rigopoulou D., Baker A. J., Iserlohe C., Tecza M., 2002, ApJ, 580, 73

Tadhunter C. N., Scarrott S. M., Draper P., Rolph C., 1992, MNRAS, 256, 53

Tadhunter C. N., Dickson R., Morganti R., Robinson T. G., Wills K., Villar-Martin M., Hughes M., 2002, MNRAS, 330, 977

Tadhunter C. N., Robinson T. G., González Delgado R. M., Wills K., Morganti R., 2005, MNRAS, 356, 480

van Breugel W. J. M., Stanford S. A., Spinrad H., Stern D., Graham J. R., 1998, ApJ, 502, 614

West M. J., 1994, MNRAS, 268, 79

Willott C. J., Rawlings S., Blundell K. M., Lacy M., 1999, MNRAS, 309, 1017

Wills K. A., Tadhunter C. N., Robinson T. G., Morganti R., 2002, MNRAS, 333, 211

Zirm A. W., Dickinson M., Dey A., 2003, ApJ, 585, 90

This paper has been typeset from a TEX/LATEX file prepared by the author.